Forschungsbericht 2024-30

Applicability of the Lattice Boltzmann Method to Simulate Fluid Flows in Rocket Engines

Tobias Traudt

Deutsches Zentrum für Luft- und Raumfahrt
Institut für Raumfahrtantriebe
Lampoldshausen

Deutsches Zentrum
DLR für Luft- und Raumfahrt

Forschungsbericht 2024-30

Lattice Boltzmann Method, transient, chilldown, compressible, two-phase, rocket engine

Tobias Traudt

Deutsches Zentrum für Luft- und Raumfahrt
Institut für Raumfahrtantriebe
Standort

103 Seiten
15 Bilder
5 Tabellen
50 Literaturstellen

Deutsches Zentrum
DLR für Luft- und Raumfahrt

Herausgeber:

Deutsches Zentrum
für Luft- und Raumfahrt e. V.
Wissenschaftliche
InformationLinder Höhe
D-51147 Köln

ISSN 1434-8454
ISRN DLR-FB-2024-30
Erscheinungsjahr 2025
DOI: 10.57676/szpe-kg36

D 93 (Dissertation Universität Stuttgart)

Erklärung des Herausgebers:

Lattice Boltzmann Method, transient, chilldown, compressible, two-phase, rocket engine

Tobias TRAUDT
DLR, Institut für Raumfahrtantriebe, Lampoldshausen

Dissertation Universität Stuttgart
Über die Anwendbarkeit der Lattice Boltzmann Methode zur Strömungssimulation in Raketentriebwerken

Die wichtigste Grundlage des Raumtransports ist, dass das Gewicht der Struktur auf ein Minimum reduziert und die Energiedichte auf ein Maximum angehoben wird. Diese Anforderungen sind bis zu einem gewissen Grad widersprüchlich und führen zu Lösungen an der Grenze der technischen Machbarkeit. Für einen reibungslosen Betrieb des Triebwerks ist große Sorgfalt in der Entwurfsphase erforderlich, weswegen umfassende CFD Simulationen instationärer Phänomene durchgeführt werden .
Diese Arbeit konzentriert sich auf die besonderen Herausforderungen, die mit kryogenen Treibstoffen in Raketentriebwerken verbunden sind. Die Temperaturgradienten während der Abkühlungsphase vor dem Start führen zur intensiven Verdampfung des Treibstoffs wodurch oft hohe Druckstöße und Gasströmungen mit hoher Geschwindigkeit ausgelöst werden, was den sicheren Start des Triebwerks erschwert.
Die Lattice-Boltzmann-Methode (LBM) verspricht, qualitativ hochwertige Ergebnisse in kurzer Zeit zu liefern. Sie ist bekannt für ihre Effektivität bei der Behandlung von Zweiphasenströmungen und wurde aufgrund ihres Potenzials ausgewählt, die charakteristischen steilen Temperaturgradienten, Verdampfungseffekte und kompressiblen Strömungen dieser Systeme zu bewältigen. Aus der Literatur wurde ein thermisches Zweiphasenmodell ausgewählt, das einen sogenannten multi-speed Finite-Differenzen-Ansatz mit einem zusätzlichen Kraftterm für die mathematische Beschreibung des Phasenwechsels enthält.
Die Validierung des Modells erfolgt durch Simulationen verschiedener Szenarien, die jeweils unterschiedliche für Raketentriebwerke relevante Phänomene darstellen. Der erste Validierungsfall ist die sogenannte „driven cavity“, um zu zeigen, dass das gewählte LBM in der Lage ist, eine inkompressible, stationäre Einphasenströmung korrekt zu reproduzieren. Die Verdampfung einer einzelnen Blase auf einer beheizten Oberfläche zeigt, dass der Code in der Lage ist spontane Verdampfung zu simulieren. Eine Riemannsche Stoßrohrsimulation wurde gewählt als Testfall für Schocks und Überschallströmungen. Schließlich wurde das Modell zur Simulation von Druckstößen mit flüssigem Stickstoff eingesetzt. Das LBM ist in der Lage die wichtigsten Strömungsmerkmale und dynamischen Verhaltensweisen in diesen Fällen wiederzugeben. Dabei ist die geringe Fehlerrate beim beim Riemannschen Stoßrohrs hervorzuheben. Allerdings wurden kleinere Mängel bei der Dämpfung des Drucks und der Vorhersage des Spitzendrucks während der Druckstoßsimulationen festgestellt.
Den Abschluss der Arbeit bildet die Simulation eines mit Blasen gefüllten Kanals, um die Dämpfung der Druckwellen aufgrund der Mehrfachstreuung der Wellen in der Blasenwolke zu untersuchen. Das LBM konnte die in diesem Szenario beobachtete starke Abschwächung der Druckwellen effektiv abbilden. Es wurden jedoch auch Einschränkungen festgestellt, darunter die Notwendigkeit eines verbesserten Modells für reale Gase, da sich die dem gewählten Modell zu Grunde liegende van-der-Waals-Zustandsgleichung als einschränkend erwies. Außerdem müssen die Stabilität des Modells und die Genauigkeit der Druckwellendämpfung verbessert werden.
Insgesamt haben die LBM-Simulationen das Potenzial der Methode für die Bewältigung der physikalischen Herausforderungen im Zusammenhang mit Flüssigkeitsströmungen in Raketentriebwerken gezeigt. Die Arbeit unterstreicht die Bedeutung eines sorgfältigen Simulationsaufbaus, da die LBM-Gleichungen inhärent ihre eigenen Fluideigenschaften beschreiben, was die Abbildung physikalischer Fluideigenschaften über Ähnlichkeitsgesetze und nichtdimensionale Zahlen, wie die Reynolds-Zahl und das entsprechende Zustandsprinzip, erforderlich macht. Während letzteres für einzelne atomare Gase genau ist, wird es bei asymmetrischeren Flüssigkeitsmolekülen ungenauer.

Lattice Boltzmann Method, transient, chilldown, compressible, two-phase, rocket engine

(Published in English)

Tobias TRAUDT
German Aerospace Center (DLR), Institute of Space Propulsion, Lampoldshausen

Doctoral Thesis University of Stuttgart

Applicability of the Lattice Boltzmann Method to Simulate Fluid Flows in Rocket Engines

Space Transportation is only feasible when structure weight is reduced down to the minimum and energy density brought to the maximum limit. These requirements are to a certain extent contradicting and lead to solutions at the technical limit. Great effort in the design phase is necessary to ensure an unproblematic operation. For this reason, high fidelity simulations of unsteady phenomena are used extensively in the design and operation of a rocket engine. This research focuses on the specific challenges associated with cryogenic liquids in rocket engines, where significant temperature gradients and evaporation phenomena occur during the chilldown phase prior to engine start-up. The chilldown process often results in high-pressure surges and high-velocity gas flows, complicating the safe start-up of the engine.
The Lattice Boltzmann Method promises to yield high quality results in a fast time. The LBM, known for its effectiveness in handling two-phase flows, was selected for its potential to manage the steep temperature gradients, evaporation, and compressible flows characteristic of these systems. A thermal two-phase model incorporating a multi-speed finite difference approach and an additional force term was chosen from the literature.
Validation of the model was conducted through simulations of various scenarios, each representing different phenomena of interest in rocket engines. The first validation case is the driven cavity flow to show that the chosen LBM is capable to correctly reproduce incompressible steady single-phase flow. The evaporation of a single bubble on a heated surface was chosen because the code should be able to handle instantaneous evaporation as is the case during chilldown. A Riemann shock tube simulation shows the capability of the model to handle shocks and supersonic flows and finally the model is used to simulate pressure surges with liquid nitrogen.
The results demonstrated that the LBM accurately reproduced the main flow features and dynamic behaviours in these cases. Specifically, it showed good agreement in the driven cavity flow, effective simulation of evaporation processes, and low error rates in replicating the characteristics of a Riemann shock tube. However, minor shortcomings were noted in the pressure attenuation and peak pressure prediction during pressure surge simulations.
The work concludes with a simulation of a duct filled with bubbles to study the attenuation of pressure waves due to multiple wave scattering in the bubble cloud. The LBM effectively captured the strong pressure wave attenuation observed in this scenario. However, limitations were identified, including the need for an improved real gas model, as the current model's adherence to the van-der-Waals equation of state was found to be restrictive. Furthermore, the stability of the model and the accuracy of pressure wave attenuation require enhancement.
Overall, the LBM simulations demonstrated the method's potential for addressing the physical challenges associated with fluid flows in rocket engines. The study emphasizes the importance of careful simulation setup, as LBM equations inherently describe their own fluid properties, necessitating the mapping of physical fluid properties via similarity laws and non-dimensional numbers, such as the Reynolds number and the corresponding states principle. While the latter is accurate for single atomic gases, it becomes less precise with more asymmetrical fluid molecules.

Applicability of the Lattice Boltzmann Method to Simulate Fluid Flows in Rocket Engines

A thesis accepted by the Faculty of Aerospace Engineering and Geodesy of the University of Stuttgart in fulfilment of the requirements for the degree of Doctor of Engineering Sciences (Dr.-Ing.)

by Tobias Traudt
born in Neunkirchen (Saar)

Main referee:	Prof. Dr.-Ing. Stefan Schlechtriem
Co-referee:	Prof. Dr.-Ing. habil. Bernhard Weigand
Day of defense:	Dec. 18th 2024

Institute of Space Systems
University of Stuttgart
2025

Table of Contents

List of Figures

List of Tables

Nomenclature

f	: distribution function
t	: time
$\vec{x}$	: coordinate
$\vec{\xi}$	: particle velocity vector
τ	: relaxation time
f^{eq}	: equilibrium distribution function
c	: magnitude of velocity
n,ρ	: density
$\vec{u}$	: velocity vector
e	: internal energy
R	: specific gas constant
T	: temperature
F	: weight
s	: equilibrium distribution
A	: weighting factor
Δs	: lattice spacing
Δt	: time step
$\mathcal{F}$	: flux
Ψ	: flux limiter
Θ	: smoothness function
$\delta_{\alpha\beta}$	: Kronecker delta function

μ : viscosity

κ_e : heat conductivity

κ : ratio of specific heats

I : interparticle force term

p,P : pressure

Subscripts

k : index for absolute velocity

i : direction index

α, β ... : vector component

List of Abbreviations

BBBC	Bounce Back Boundary Condition
BC	Boundary Condition
BE	Boltzmann Equation
BGK	Bhatnagar-Gross-Krook
CEE	Chapman-Enskog Expansion
CFD	Computational Fluid Dynamics
CFL	Courant-Friedrichs-Levy Condition
DxQy	Dimension x and number of velocities y of the LBM grid
EOS	Equation of State
ES	Equation System
FDLBM	Finite Difference Lattice Boltzmann Model
FE	Free Energy Model
FHP	Frisch, Hasslacher, Pomeau
LB	Lattice Boltzmann
LBM	Lattice-Boltzmann Method
LGA	Lattice Gas Automaton
LN2	Liquid Nitrogen
LOX	Liquid Oxygen
LS	Level Set Method
lu	Lattice Unit
MFM	Mean Field Model

NIST	National Institute of Standards and Technology
NSE	Navier-Stokes Equations
PS	Passive Scalar Model
Re	Reynolds Number
SC	Shan Chen Model
SSME	Space Shuttle Main Engine
TF	Two-Phase Flow
ts	Time Step
TSM	Temperature Shift Model
vdW	van der Walls
VOF	Volume of Fluid Method
WT	Watari Tsutahara Model
WTG	Watari Tsutahara Gonella Model

Abstract

Space Transportation is only feasible when structure weight is reduced down to the minimum and energy density brought to the maximum limit. These requirements are to a certain extent contradicting and lead to solutions at the technical limit. Great effort in the design phase is necessary to ensure an unproblematic operation. For this reason, high fidelity simulations of unsteady phenomena are used extensively in the design and operation of a rocket engine. This research focuses on the specific challenges associated with cryogenic liquids in rocket engines, where significant temperature gradients and evaporation phenomena occur during the chilldown phase prior to engine start-up. The chilldown process often results in high-pressure surges and high-velocity gas flows, complicating the safe start-up of the engine.

The Lattice Boltzmann Method promises to yield high quality results in a fast time. The LBM, known for its effectiveness in handling two-phase flows, was selected for its potential to manage the steep temperature gradients, evaporation, and compressible flows characteristic of these systems. A thermal two-phase model incorporating a multi-speed finite difference approach and an additional force term was chosen from the literature.

Validation of the model was conducted through simulations of various scenarios, each representing different phenomena of interest in rocket engines. The first validation case is the driven cavity flow to show that the chosen LBM is capable to correctly reproduce

incompressible steady single-phase flow. The evaporation of a single bubble on a heated surface was chosen because the code should be able to handle instantaneous evaporation as is the case during chilldown. A Riemann shock tube simulation shows the capability of the model to handle shocks and supersonic flows and finally the model is used to simulate pressure surges with liquid nitrogen.

The results demonstrated that the LBM accurately reproduced the main flow features and dynamic behaviours in these cases. Specifically, it showed good agreement in the driven cavity flow, effective simulation of evaporation processes, and low error rates in replicating the characteristics of a Riemann shock tube. However, minor shortcomings were noted in the pressure attenuation and peak pressure prediction during pressure surge simulations.

The work concludes with a simulation of a duct filled with bubbles to study the attenuation of pressure waves due to multiple wave scattering in the bubble cloud. The LBM effectively captured the strong pressure wave attenuation observed in this scenario. However, limitations were identified, including the need for an improved real gas model, as the current model's adherence to the van-der-Waals equation of state was found to be restrictive. Furthermore, the stability of the model and the accuracy of pressure wave attenuation require enhancement.

Overall, the LBM simulations demonstrated the method's potential for addressing the physical challenges associated with fluid flows in rocket engines. The study emphasizes the importance of careful simulation setup, as LBM equations inherently describe their own

fluid properties, necessitating the mapping of physical fluid properties via similarity laws and non-dimensional numbers, such as the Reynolds number and the corresponding states principle. While the latter is accurate for single atomic gases, it becomes less precise with more asymmetrical fluid molecules.

Keywords: Lattice Boltzmann Method, transient, chilldown, compressible, two-phase, rocket engine

Zusammenfassung

Die wichtigste Grundlage des Raumtransports ist, dass das Gewicht der Struktur auf ein Minimum reduziert und die Energiedichte auf ein Maximum angehoben wird. Diese Anforderungen sind bis zu einem gewissen Grad widersprüchlich und führen zu Lösungen an der Grenze der technischen Machbarkeit. Für einen reibungslosen Betrieb des Triebwerks ist große Sorgfalt in der Entwurfsphase erforderlich, weswegen umfassende CFD Simulationen instationärer Phänomene durchgeführt werden .

Diese Arbeit konzentriert sich auf die besonderen Herausforderungen, die mit kryogenen Treibstoffen in Raketentriebwerken verbunden sind. Die Temperaturgradienten während der Abkühlungsphase vor dem Start führen zur intensiven Verdampfung des Treibstoffs wodurch oft hohe Druckstöße und Gasströmungen mit hoher Geschwindigkeit ausgelöst werden, was den sicheren Start des Triebwerks erschwert.

Die Lattice-Boltzmann-Methode (LBM) verspricht, qualitativ hochwertige Ergebnisse in kurzer Zeit zu liefern. Sie ist bekannt für ihre Effektivität bei der Behandlung von Zweiphasenströmungen und wurde aufgrund ihres Potenzials ausgewählt, die charakteristischen steilen Temperaturgradienten, Verdampfungseffekte und kompressiblen Strömungen dieser Systeme zu bewältigen. Aus der Literatur wurde ein thermisches Zweiphasenmodell ausgewählt, das einen sogenannten multi-speed Finite-Differenzen-Ansatz mit

einem zusätzlichen Kraftterm für die mathematische Beschreibung des Phasenwechsels enthält.

Die Validierung des Modells erfolgt durch Simulationen verschiedener Szenarien, die jeweils unterschiedliche für Raketentriebwerke relevante Phänomene darstellen. Der erste Validierungsfall ist die sogenannte „driven cavity“, um zu zeigen, dass das gewählte LBM in der Lage ist, eine inkompressible, stationäre Einphasenströmung korrekt zu reproduzieren. Die Verdampfung einer einzelnen Blase auf einer beheizten Oberfläche zeigt, dass der Code in der Lage ist spontane Verdampfung zu simulieren. Eine Riemannsche Stoßrohrsimulation wurde gewählt als Testfall für Schocks und Überschallströmungen. Schließlich wurde das Modell zur Simulation von Druckstößen mit flüssigem Stickstoff eingesetzt. Das LBM ist in der Lage die wichtigsten Strömungsmerkmale und dynamischen Verhaltensweisen in diesen Fällen wiederzugeben. Dabei ist die geringe Fehlerrate beim beim Riemannschen Stoßrohrs hervorzuheben. Allerdings wurden kleinere Mängel bei der Dämpfung des Drucks und der Vorhersage des Spitzendrucks während der Druckstoßsimulationen festgestellt.

Den Abschluss der Arbeit bildet die Simulation eines mit Blasen gefüllten Kanals, um die Dämpfung der Druckwellen aufgrund der Mehrfachstreuung der Wellen in der Blasenwolke zu untersuchen. Das LBM konnte die in diesem Szenario beobachtete starke Abschwächung der Druckwellen effektiv abbilden. Es wurden jedoch auch Einschränkungen festgestellt, darunter die Notwendigkeit eines verbesserten Modells für reale Gase, da sich die dem gewählten

Modell zu Grunde liegende van-der-Waals-Zustandsgleichung als einschränkend erwies. Außerdem müssen die Stabilität des Modells und die Genauigkeit der Druckwellendämpfung verbessert werden.

Insgesamt haben die LBM-Simulationen das Potenzial der Methode für die Bewältigung der physikalischen Herausforderungen im Zusammenhang mit Flüssigkeitsströmungen in Raketentriebwerken gezeigt. Die Arbeit unterstreicht die Bedeutung eines sorgfältigen Simulationsaufbaus, da die LBM-Gleichungen inhärent ihre eigenen Fluideigenschaften beschreiben, was die Abbildung physikalischer Fluideigenschaften über Ähnlichkeitsgesetze und nichtdimensionale Zahlen, wie die Reynolds-Zahl und das entsprechende Zustandsprinzip, erforderlich macht. Während letzteres für einzelne atomare Gase genau ist, wird es bei asymmetrischeren Flüssigkeitsmolekülen ungenauer.

Schlüsselwörter: Lattice-Boltzmann-Methode, instationär, Chill-down, kompressibel, zweiphasig, Raketentriebwerk

1 Introduction

Simulation of multiphase flows is of special interest for a lot of applications. These are for example loss of coolant accidents in nuclear power plants, or flows of cryogenic liquid in rocket engines. While the first one deals with surfaces at temperatures well above ambient temperature, cryogenic liquids are well below ambient temperature. For both the temperature gradients between the “hot” wall and the “cold” liquid are typically in the same order of magnitude.

In this work we focus on cryogenic liquids for rocket engines. Cryogenic liquids are usually stored at their saturation properties, because even if tere is insulation heat from the environment is conducted into the fluid. When the fluid comes in contact with walls at ambient conditions, as is the case for the chilldown of rocket components prior to launch, voracious evaporation will take place. The boil off of liquid produces a lot of gas, which will lead to very high velocities of the gas phase, eventually blocking the pipe diameter, when sonic velocity is reached.

During the operation of a launcher, the chilldown is usually done before the start-up of the engine itself. This way the evaporation of fuel or oxidizer is kept to a minimum in the feedlines, the components, as well as in the so-called engine dome, which distributes the liquids to the injection elements. However, the chilldown will not bring every component of the engine below the saturation temperature of the liquids and the evaporation processes play a major role

during the start-up of the engine. During the development of the Space Shuttle Main Engine (SSME) for example, great care had to be taken in order not to exceed the pressure limits of the components at start-up. The valve sequences had to be chosen in such a way that pressure ramp up in the gas generator as well as the combustion chamber did not coincide with pressure spikes caused by boil off effects (Biggs, 1989).

For these reasons, a numerical code which is supposed to numerically simulate propellant flows in rocket engine feedlines needs to be able to simulate temperature, heat-transfer, evaporation and steep pressure gradients. The significant evaporation during chill-down can even lead to high velocity gas phase flows close to Mach 1. The highly non-homogeneous two-phase flows benefit from a numerical technique which is able to handle compressible flows. All of these aspects are difficult for numerical codes and usually Navier-Stokes Solvers are used to simulate these kinds of problems in order to increase the knowledge about the complicated processes inside of rocket engines. Apart from simulating fluid flows by solving the Navier-Stokes Equations directly, there is another approach, the so-called Lattice-Boltzmann Method (LBM). The literature about the LBM is optimistic about its use for two phase flow for example and usually states the very good and fast results which have been obtained by it (Gonnella, et al., 2007), (Yuan & Schäfer, 2006), (Chen & Doolen, 1998), (Shan & Chen, 1993), (Shan & Chen, 1994), (Kupershtokh, et al., 2009), (Zhang & Chen, 2003), (Zhang, et al., 2004). This works aim is to give on overview on the existing

models, choose a model which is suitable for the aforementioned challenges, implement it and simulate validation cases in order to investigate the applicability of the LBM to fluid flows in rocket engines feed systems.

2 Simulation of Multiphase Flows with the LBM

Multiphase flows consist of one or more substances in its solid, liquid and/or gaseous phase. In this work we focus on two-phase (liquid and gaseous) flow of typical rocket engine propellants like liquid oxygen (LOX).

The LBM uses a mesoscopic particle system for the prediction of fluid flows because the number of particles is between the microscopic scale of the Boltzmann equation and the macroscopic averaged continuum viewpoint of the NSE.

What makes the LBM interesting for the simulation of multiphase flows is its inherent representation of the phase interface, which lacks the need for special interface tracking methods usually used in direct Navier-Stokes solvers like the volume of fluid (VOF) or level set (LS) method. This is due to its microscopic level realization of nonideal gas equations of state, which spontaneously generates first order phase transitions (Zhang & Chen, 2003).

Another feature of the LBM is its capability to handle very complex geometries. The reason for this is twofold. On one hand there are boundary conditions which are very easy to implement and set up (see section 3.1.1) and on the other hand, the grid generation for the LBM is a fast process, because usually square or cubic elements are used.

The following chapters will present the LBM in detail and try to give explanations for its use.

2.1 History of the LBM, the Lattice Gas Automaton (LGA)

According to (Sukop, 2006) the LBM originated out of the so-called Lattice gas automaton (LGA) which was a simplified particle simulation to describe the flow of fluids. The first LGA that was able to solve the NSE was the FHP model, named after the authors Frisch, Hasslacher and Pomeau (Frisch, et al., 1986). The LGA uses a hexagonal grid on which the particles move. On each node of the grid a value of 0 indicates a missing particle and an existing particle is indicated by 1. Since the grid is equally spaced and the time step is fixed the possible directions of the particles are reduced to six and the magnitude of the velocity to two values. The particles move to any of these six directions, and since every node has six neighbours the "worst case" is a maximum of six particles which can be found at a single node. Usually the distance between each node is called lattice unit (lu) (see Figure 1) and the abbreviation for the time step is ts, which makes *lu/ts* the unit of the velocity. So, the discrete magnitudes for the velocity are 1 *lu/ts* and of course 0 *lu/ts*.

At every time step the particles move to a new lattice node and collide and scatter according to collision rules.

The FHP-Model only considers two types of collisions. On the one hand there is the collision between two particles and on the other hand there is the collision between 3 particles approaching one another in an angle of 120°.

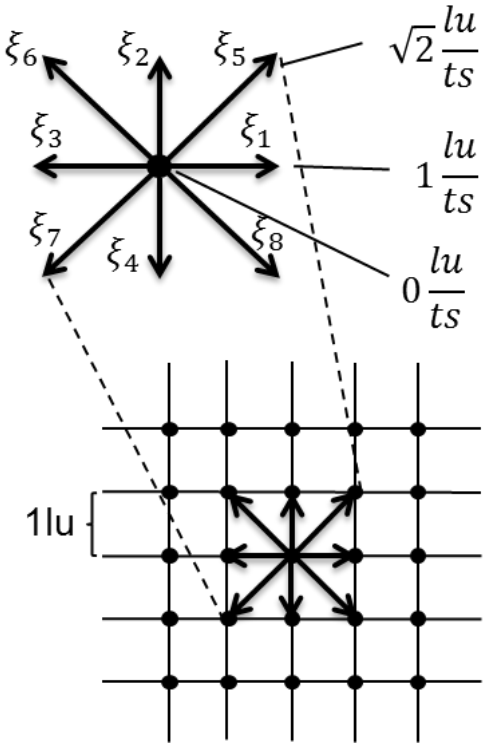

Figure 1: Quadratic Grid of the LBM

The collision must satisfy mass and momentum conservation. Because the particles all have the same velocities the momentum conservation in fact reduces to a conservation of the vector sum of the velocities. This leads to the conclusion that head on collisions of two particles have three possible post-collision states, because all velocity vectors of particles pointing away from the centre have a net momentum of zero. In the same way head on collisions of three particles have two possible outcomes. Which outcome is chosen during simulation is decided randomly by the algorithm. The fact that particles have several different directions after the collision might look strange at first. It might help thinking of two spheres that do not always collide perfectly head on and consequently do

not travel in the exact opposite direction after collision. The randomness in collisions introduces a lot of noise into the procedure which is essential in the ability of the LGA to simulate fluids, but it also makes temporal and/or spatial averaging necessary to obtain a smooth flow field (Sukop, 2006).

A simple boundary condition is the bounce back boundary condition, where a particle hitting the wall gets re-emerged into the flow in the direction where it came from.

For simulating a driving force one can give some particles a momentum into the desired direction to obtain this effect.

According to (Chen & Doolen, 1998) the governing equation for the LGA is

$$n_a\left(\vec{x} + \vec{\xi}_a \Delta t, t + \Delta t\right) = n_a(\vec{x}, t) + \Omega_a\left(n(\vec{x}, t)\right) \qquad (2.1)$$

Where n is the Boolean for the particle, with $n = 0$ means particle not present, a is an index referring to the direction where the particle is coming or going to, $\vec{x}$ is the position of the actual node, $\vec{\xi}$ is the velocity of the particle a, t is the time and Ω is the so called collision operator. See Figure 1 for more details on the velocities and the subscript a.

Amazingly even with this simple model simulations of a fluid flow are possible but only with limited accuracy. However, the underlying principles help understanding the LBM, which shall be presented in the next chapter.

2.2 Basic Equation of the LBM

The main evolutionary step that has been taken from the LGA to the LBM is that instead of using particles itself the particles were substituted by a particle distribution function f. Instead of moving the particles themself from one node to another and instead of taking particle-particle interactions into account, the average of an ensemble of particles is used, while preserving the kinetic nature of the LBM (Chen & Doolen, 1998). This means mathematically that the Booleans n for the particles in equation 2.1 are replaced by the distribution function f.

Another way to obtain the Lattice-Boltzmann equations is the discretization of the Boltzmann equation (see equation 2.2) in time and space. In the BE, f is the microscopic distribution function of a particle system of N particles. Each particle has its own distribution function that is dependent on the time t and the microscopic velocity of the particle $\vec{\xi}$, $\mathrm{f^N}(t, \vec{x}^{(1)}, \vec{\xi}^{(1)}, \dots, \vec{x}^{(N)}, \vec{\xi}^{(N)})$. The distribution function in the BE gives the probability that the system of N particles is in the state $\left(\vec{x}^{(1)}, \vec{\xi}^{(1)}, \dots, \vec{x}^{(N)}, \vec{\xi}^{N}\right)$ at the time t.

$$\frac{\partial f}{\partial t} + \vec{\xi} \cdot \frac{\partial f}{\partial \vec{x}} = -\frac{1}{\tau}(f - f^{eq}) = \Omega \qquad (2.2)$$

The term on the right side is the collision operator Ω. Here it is presented in the very easy and therefore popular form named Bhatnagar-Gross-Krook approximation or in short BGK. The BGK approximation is dependent on the relaxation time τ which gives a measure for the time it takes the system to reach its equilibrium

state f^{eq}. The derivative $\delta f/\delta t$ is equal to zero when there is no variance in density and velocity over the volume of interest and the equilibrium distribution function becomes the Maxwell distribution.

$$f^{eq} = \frac{\rho}{(2\pi c_s^2)^{\frac{d}{2}}} \exp\left(-\frac{\left(\vec{\xi} - \vec{u}\right)^2}{2c_s^2}\right) \tag{2.3}$$

Where c_s is the speed of sound, ρ is the macroscopic fluid density, $\vec{u}$ is the macroscopic fluid velocity and d is the dimension of the space in consideration. The equilibrium distribution function is chosen in a way so that the mass and momentum conservation is ensured (Gonnella, et al., 2007).

The BE is playing a major role in the history of thermodynamics because it founded a new branch of it, the statistic thermodynamics. With it, it was possible to give explanations for macroscopic fluid properties from a microscopic viewpoint using only classical mechanics (Sukop, 2006).

Obviously, the BE needs to be discretized because it would not be possible to simulate all particles in a fluid in a reasonable amount of time. The reason is the number of particles which is in the order of $\sim 10^{23}$ for one mole of gas (22,4l under standard conditions). Apart from this there is an infinite possibility for the directions and magnitudes of the velocities of the particles. For simplicity and to get an overview over the scheme the following equations will be derived for a quadratic two-dimensional grid.

In the LBM literature a special naming scheme for the different grids has been established. In the form DxQy it gives information about the dimension x and the number of velocity vectors y of the grid. For a two-dimensional grid with 9 velocity vectors, as it is shown in Figure 1, this yields the name D2Q9. Respectively the name for a three-dimensional grid with 19 possible velocity vectors is D3Q19.

The discretization of the BE with respect to the lattice spacing lu and the time step Δt finally yields the most often used form of the main equation for the LBM

$$f_a\left(\vec{x} + \vec{\xi}_a \Delta t, t + \Delta t\right) = f_a(\vec{x}, t) - \frac{\Delta \mathrm{t}}{\tau}\left[f_a(\vec{x}, t) - f_a^{eq}(\vec{x}, t)\right] \tag{2.4}$$

The discretization of the BE will be presented in detail in section 2.4.

As mentioned in section 2.1 one obtains the same relation by substituting the Boolean n in equation 2.1 by the distribution function f. The rest of the variables and indices are the same, except for the collision operator which is replaced here by the BGK approximation.

The BGK approximation is dependent on the distribution function at the current time and node $f_a(\vec{x}, t)$ and the equilibrium distribution function $f_a^{eq}(\vec{x}, t)$. f_a^{eq} also needs to be discretized and is according to (Sofonea & Sekerka, 2003)

$$f_a^{eq} = w_a \rho(\vec{x}) \left[1 + \frac{\vec{\xi} \cdot \vec{u}}{\chi c^2} + \frac{\left(\vec{\xi} \cdot \vec{u}\right)^2}{2\chi^2 c^4} - \frac{\vec{u}^2}{2\chi c^2} \right] \tag{2.5}$$

f_a^{eq} is dependent on the macroscopic fluid density ρ, the speed of sound on the lattice $c = 1\ lu/\Delta t$, and the known LBM variables. The factor χ has different values for different grids. For the D2Q9 grid it is equal to $1/3$ for example. The variable w_a denotes a weight which besides being dependent on the node a which the distribution function belongs to, is also dependent on the grid that it is used for. This means that for the D2Q9 grid w_a is $4/9$ for the rest particle ($a = 0$), $1/9$ for $a = 1,2,3,4$, and $1/36$ for $a = 5,6,7,8$.

As will be shown in section 2.4 one limitation of the classical LBM is the limitation to small flow speeds. The condition

$$\frac{\mathrm{u_{phys}}}{u_{LBM}} \ll 1 \tag{2.6}$$

needs to be satisfied. In literature a maximum value of $u_{phys} \leq 0.1 u_{LBM}$ is recommended. Where u_{LBM} is the speed of sound on the lattice

$$c = \frac{\partial s}{\partial t} \tag{2.7}$$

To clarify the meaning of the subscripts it helps to think of it as a direction specific density, which has a different value for all possible directions of the node (Figure 2). In chapter 3.1 where the numerical implementation will be explained it becomes clear that the distribution functions $f_a, a = 0, \ldots, 8$ are present at each node but

they get "streamed" to the neighbouring nodes at the next iteration step according to the indices. During the streaming step, $f_a(\vec{x} + \vec{\xi}_a \Delta t)$ is replaced by $f_a(\vec{x})$ (Alexander, et al., 1993).

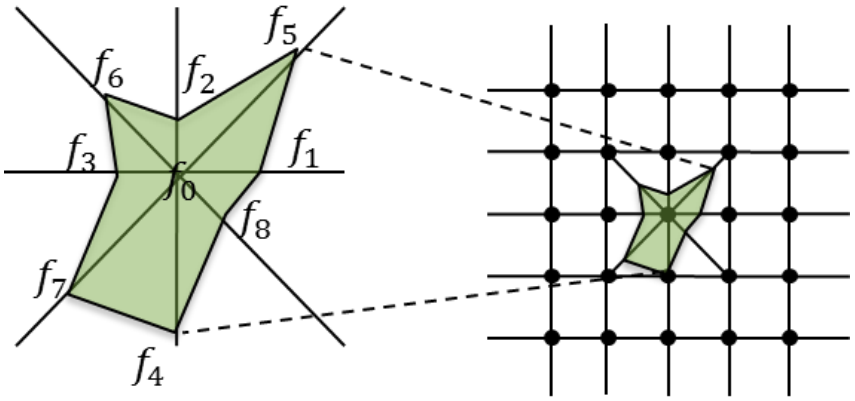

Figure 2: Naming of the distribution functions for the D2Q9

Correspondingly every node receives a new set of nine distributions at every time step from its neighbouring nodes.

Due to its historic relations to the LGA (see chapter 2.1), the most often used form of the LBM is the one shown in equation 2.4, which obviously is a first order finite difference scheme, also called first order upwind or forward Euler scheme. In fact, the LBM is a special case of the upwind finite difference LBM, when also the relaxation term is calculated on the characteristics line (Sofonea & Sekerka, 2003), (Tölke, 2001). As shown in (Junk, et al., 2005) it is accurate to the second order in space but only to the first order in time. To overcome this, there is the possibility to solve the BE by other schemes of higher order (Sofonea & Sekerka, 2003), (Cristea &

Sofonea, 2004), nevertheless most of the literature focuses on the first order upwind scheme.

The relation between the mesoscopic distribution function f and the macroscopic variables ρ and $\vec{u}$ is given by the first and second order moments

$$\rho = \sum_{a=0}^{8} f_a \tag{2.8}$$

$$\rho\vec{u} = \sum_{a=0}^{8} f_a \vec{\xi}_a \tag{2.9}$$

(Chen & Doolen, 1998). With these equations the term direction specific density becomes clearer. The distribution function f_a can be thought of as a partial density that moves to neighbouring nodes with the velocity and direction of $\vec{\xi}_a$, while the donator node gets new partial densities from the surrounding nodes.

With all of the above the basic equation of the LBM is capable of simulating incompressible isothermal flows. The mathematical origins of these limitations and some other LBM specific characteristics is presented in the next sections. Also, an overview of sub-models is given that have been developed for the LBM to overcome shortcomings of method that are crucial for the problems under investigation later on.

2.2.1 Viscosity

In the LBM the viscosity is given by the scheme itself. For the classical LBM equation 2.4 with the BGK approximation it is

$$\nu = \chi c^2 \left(\tau - \frac{\Delta t}{2}\right), \qquad [\nu] = \frac{lu^2}{ts} \tag{2.10}$$

Where ν is the kinematic viscosity, χ is the same grid dependent factor like for equation 2.5 and τ is the relaxation time of the BGK approximation.

(Sofonea & Sekerka, 2003) showed that the viscosity of the first order upwind scheme of the classical LBM (equation 2.4) is composed of a physical value $\nu_{phys} = \chi c^2 \tau$ and a numerical value $\nu_{num} = \frac{1}{2}\chi c^2 \Delta t$ which is dependent on the time step of the scheme. (Sofonea & Sekerka, 2003) mention that there is no spurious numerical viscosity in the incompressible region if the second order upwind scheme or second order space centred scheme is used instead for approximating the time derivative of the BE.

For the classical LBM where the dimensions have been made dimensionless by the lattice spacing (1lu) and the time step, the viscosity (see equation 2.10) reduces for the D2Q9 to

$$\nu = \frac{1}{3}\left(\tau - \frac{1}{2}\right) \tag{2.11}$$

The viscosity needs to be positive for the classical LBM so the lower limit for τ is 0.5. The upper limit of the viscosity is also fixed (Buwa, et al., 2010), which leads to the valid range of τ of

$$0.5 \geq \nu \leq 2.0 \tag{2.12}$$

According to (Sofonea & Sekerka, 2003) the condition $\tau > \frac{\delta t}{2}$, which leads to $\tau > 0.5$ for $\delta t = 1$, is only required for the classical LBM and is overcome by another scheme.

The viscosity of the fluid simulated by the LBM is always higher than the physical value and the discretization has a direct impact on the fluid properties. This means that one needs to take some effort in order to correlate the physical values and the numerical simulation correctly. Here we refer to section 3.1.3 for more detail.

2.2.2 External Forces

Implementing forces in LBM is straight forward and it does not matter of which nature the force is. May it be the force acting on the fluid by gravitational acceleration or the attracting force between two neighbouring 'particles' like the ones used in some multiphase models. There are two ways to implement both.

The first way is to consider the effect of the force onto the momentum by altering the velocity by the amount $\Delta\vec{u}$.

The force can be expressed as

$$\vec{F} = m\vec{a} = m\frac{d\vec{u}}{dt} \tag{2.13}$$

Density is proportional to the mass and the relaxation time τ (Sukop, 2006) which leads to

$$\Delta\vec{u} = \frac{\tau\vec{F}}{\rho} \tag{2.14}$$

and finally, the velocity in equilibrium which is used to calculate f^{eq} is

$$\vec{u}^{eq} = \vec{u} + \Delta\vec{u} = \vec{u} + \frac{\tau\vec{F}}{\rho} \tag{2.15}$$

The second way to consider a force on the fluid is to introduce a second body force term to the right hand side of eq. 2.4 (Zhang & Chen, 2003), (Shan & Chen, 1993), (Chen & Doolen, 1998)

$$\begin{aligned} f_a\left(\vec{x} + \vec{\xi}_a \Delta t, t + \Delta t\right) \\ = f_a(\vec{x}, t) - \frac{\Delta \mathrm{t}}{\tau}\left[f_a(\vec{x}, t) - f_a^{eq}(\vec{x}, t)\right] \\ - \Omega_a^k \end{aligned} \tag{2.16}$$

with

$$\Omega_a^k = \xi_{a\alpha} \cdot F^k \tag{2.17}$$

where F^k is an effective force on the kth phase and/or component.

2.2.3 Prandtl Number

It is worthwhile to notice that the BGK limits problems to $Pr = 0.5$ (Alexander, et al., 1993). To overcome this limitation there are several possibilities, like collision operators with multiple relaxation times or by implementing a sophisticated real gas model like in section 2.6.4.2.

2.3 Relation of the LBM to the Boltzmann Equation

As mentioned before the LBM can also be derived out auf the BE by discretizing it. By looking at how the discretization of the Boltzmann Equation is done, one gets an insight in the reasons for the limitations of the LBM.

According to (Tölke, 2001) the discretization is split in two steps in order to relate the discretization errors to the correct phenomenon.

The first step is the discretizing the microscopic velocity space. This is done by reducing the distribution function $f(t, \vec{x}, \vec{\xi})$ to a discrete number of N particles that move with the velocity $\vec{\xi}_a$, which leads to

$$f\left(t, \vec{x}, \vec{\xi}\right) = f_a(t, \vec{x}), \quad a = 0, \dots, N-1 \tag{2.18}$$

the outcome of the above is the discrete BE

$$\frac{\partial f_a}{\partial t} + \vec{\xi}_a \frac{\partial f_a}{\partial \vec{x}} = -\frac{1}{\tau}(f_a - f_a^{eq}) \tag{2.19}$$

Next the equilibrium distribution function is discretized, using an Ansatz that ensures mass and momentum conservation and using the Chapman-Enskog Expansion (CEE)

$$f = f^{(0)} + \epsilon f^{(1)} + \epsilon^2 f^{(2)} + \cdots \tag{2.20}$$

where ϵ is the Knudsen number (Tölke, 2001).

Doing this introduces an error of the order $O(\epsilon^2)$ and $O(Ma^2)$ for the D3Q19. The Knudsen number ϵ which is defined as

$$\epsilon = \frac{c\tau}{L} \tag{2.21}$$

where c is a characteristic microscopic velocity and L a characteristic macroscopic length. The error $O(\epsilon^2)$ leads to the condition $\epsilon \ll 1$ or $\tau \ll \frac{L}{c}$ and so the relaxation time τ has to be smaller than a pressure wave traveling through this region. Also, transient boundary conditions have to vary in the time span $T \gg \tau$. The error of the order $O(Ma^2)$ limits the LBM to small Mach numbers, $Ma \ll 1$.

This means that the scheme is only valid for small Knudsen numbers ϵ and small Mach numbers Ma. Here the Mach number refers to the velocity on the grid.

One can show that the distribution number of the order zero $f^{(0)}$ is equal to the equilibrium distribution function f^{eq} (Sofonea & Sekerka, 2003).

Next the discrete BE is discretized in space and time. As mentioned before, for the classical LBM this is done with finite differences because of the historical relations of the LBM to the LGA. The discretization is done along the characteristics $\vec{\xi}_a$ and finally leads to the basic LBM equation already known

$$\begin{aligned} f_a\left(\vec{x} + \vec{\xi}_a \Delta t, t + \Delta t\right) \\ = f_a(\vec{x}, t) - \frac{\Delta \mathrm{t}}{\tau}\left[f_a(\vec{x}, t) - f_a^{eq}(\vec{x}, t)\right] \end{aligned} \tag{2.22}$$

This way an error of order $O(\Delta t^2)$ is introduced.

To give more insight to where the errors $O(\Delta t^2)$ and $O(\Delta \xi^2)$ come from, the next chapter gives a short overview of the derivation of the Navier-Stokes Equations.

2.4 Relation of the LBM to the Navier-Stokes Equations

The mathematics presented here are a summary of the detailed explanation given by (Tölke, 2001).

To start, equation 2.22 is expanded in a Taylor series. Inserting it in equation 2.22 again and using some simplifications, yields the actual differential equation that is solved by the classical lattice Boltzmann Equation

$$\begin{aligned} dgl_a = \frac{\partial f_a}{\partial t} + \xi_{a\alpha}\frac{\partial f_a}{\partial x_\alpha} + \frac{1}{\tau}\left(f_a - f_a^{eq}\right) \\ - \frac{\Delta t}{2\tau}\left(\frac{\partial}{\partial t} + \xi_{a\alpha}\frac{\partial}{\partial x_\alpha}\right)\left(f_a - f_a^{eq}\right) \\ + O(\Delta t^2) = 0 \end{aligned} \tag{2.23}$$

Now the equivalent differential equation is integrated with respect to the microscopic velocity space

$$\sum_a \Psi f_a d\vec{\xi} = 0 \tag{2.24}$$

where Ψ are the invariants of the collision. $\Psi_0 = 1$ gives the conservation of mass, $\Psi_{1,2,3} = \vec{\xi}$ leads to the conservation of momentum and finally $\Psi_4 = \vec{\xi}^2$ gives the equation for the conservation of energy.

Using the following relations

$$\begin{aligned} \rho &= \sum_a f_a \\ \rho u_\alpha &= \sum_a \xi_{a\alpha} f_a \\ \vec{\Pi}_{\alpha\beta} &= \sum_a \xi_{a\alpha}\xi_{a\beta} f_a \\ \sum_a f_a &= \sum_a f_a^{eq} \\ \sum_a \xi_{a\alpha} f_a &= \sum_a \xi_{a\alpha} f_a^{eq} \end{aligned} \tag{2.25}$$

But:

$$\sum_a \xi_{a\alpha}\xi_{a\beta} f_a \neq \sum_a \xi_{a\alpha}\xi_{a\beta} f_a^{eq}$$

and integrating the equivalent differential equation as said, one can easily get the equation for the conservation of mass

$$\frac{\partial \rho}{\partial t} + \frac{\partial \rho u_\alpha}{\partial x_\alpha} + O(\Delta t^2) = 0 \tag{2.26}$$

The way to derive the equation for the conservation of momentum is similar, and leads to

$$\frac{\partial \rho u_\alpha}{\partial t} + \frac{\partial \vec{\Pi}_{\alpha\beta}}{\partial x_\beta} - \frac{\Delta t}{2\tau}\frac{\partial}{\partial x_\beta}(\vec{\Pi}_{\alpha\beta} - \vec{\Pi}_{\alpha\beta}^{eq}) + O(\Delta t^2) = 0 \tag{2.27}$$

To determine the unknown momentum flux tensor $\vec{\Pi}_{\alpha\beta}$, a Taylor series expansion is carried out. Neglecting the second order terms introduces an error of $O(\epsilon^2)$

$$\frac{\partial \rho u_\alpha}{\partial t} + \frac{\partial}{\partial x_\beta}\left[\vec{\Pi}^{eq}_{\alpha\beta} + \epsilon\left(1 - \frac{\Delta t}{2\tau}\right)\vec{\Pi}^{(1)}_{\alpha\beta}\right] + O(\Delta t^2) + O(\epsilon^2) = 0 \tag{2.28}$$

Now the use of the deviatoric stress Tensor $S_{\alpha\beta}$, the definition of the deviartoric stress tensor for the NSE, the dynamic viscosity μ and the definition of the equilibrium momentum flux tensor $\vec{\Pi}^{eq}_{\alpha\beta}$

$$\begin{gathered} S_{\alpha\beta} = -\epsilon\left(1 - \frac{\Delta t}{2\tau}\right)\vec{\Pi}^{(1)}_{\alpha\beta} \\ S_{\alpha\beta} = \mu\left(\frac{\partial u_\alpha}{\partial x_\beta} + \frac{\partial u_\beta}{\partial x_\alpha}\right) + \mu'\frac{\partial u_\gamma}{\partial x_\gamma}\delta_{\alpha\beta}, \quad \mu' = \frac{2}{3}\mu \\ \mu = c^2\rho\left(\frac{\tau}{3} - \frac{\Delta t}{6}\right) \\ \vec{\Pi}^{eq}_{\alpha\beta} = \mathrm{c}^2\rho\delta_{\alpha\beta} + \rho u_\alpha u_\beta = p\delta_{\alpha\beta} + \rho u_\alpha u_\beta \end{gathered} \tag{2.29}$$

finally lead to the Navier-Stokes equation for the conservation of momentum

$$\begin{aligned} &\frac{\partial \rho u_\alpha}{\partial t} + \frac{\partial}{\partial x_\beta}\left[p\delta_{\alpha\beta} + \rho u_\alpha u_\beta\right] \\ &\quad + \mu\frac{\partial}{\partial x_\beta}\left[\left(\frac{\partial u_\alpha}{\partial x_\beta} + \frac{\partial u_\beta}{\partial x_\alpha}\right) + \frac{2}{3}\frac{\partial u_\gamma}{\partial x_\gamma}\delta_{\alpha\beta}\right] \\ &\quad + O(\Delta t^2) + O(\epsilon^2) = 0 \end{aligned} \tag{2.30}$$

2.5 Isothermal Multi-Phase Models

The classical LBM is isothermal which might be a reason why the first multi-phase models for the LBM appearing in literature were isothermal models, too. Of this kind of models, the most often used is the model of (Shan & Chen, 1993), (Shan & Chen, 1994). Its isothermal nature restricts its use to specific problems of transient cryogenic flows, but because it is simple in nature and used frequently in literature it is presented in short in the next section.

2.5.1 Shan & Chen Model

The SC Model uses the second approach to implement the model. It expands the collision term Ω with an additional body force term.

The force F^k represents an interaction between the phases.

$$F^k = -\sum_{k'}\sum_{a} V_{kk'}(x_\alpha, x_\alpha + \xi_{a\alpha}\Delta t)\xi_{a\alpha} \tag{2.31}$$

where $V_{kk'}$ is an interaction pseudopotential between different phases (or components).

$$V_{kk'}(x_\alpha, x'_\alpha) = G_{kk'}\,(x_\alpha, x'_\alpha)\Phi^k(x_\alpha)\Phi^{k'}(x'_\alpha) \tag{2.32}$$

Here $\Phi^k(x_\alpha)$ is a function of density for the k-th phase at the position x, or the k'-th phase at the position x' respectively, which means that each phase and/or component has its own grid. According to (He & Doolen, 2002) a possible choice for $\Phi^k(x_\alpha)$ would be $\Phi^k(x_\alpha) = \rho$, but this neglects the repulsive force of the interaction force, leading to a density tending to infinity. For this reason (Shan

& Chen, 1993) choose $\Phi^k(x_\alpha) = \rho_0 \left[1 - \exp\left(-\frac{\rho}{\rho_0}\right)\right]$, which is proportional to small values of ρ and tends to a constant for large values of ρ (Sukop, 2006), (He & Doolen, 2002).

$G_{kk'}$ is a greens function and satisfies $G_{kk'} = G_{k'k}$ (Yuan & Schäfer, 2006). It is the strength of the interaction and is sometimes referred to as an inverse temperature.

The SC Model is easy to implement and gives good results. However, it has some disadvantages, namely

- The LBM equations itself remain isothermal. Apart from the obvious negative implications, this is reported to be an advantage in terms of numeric stability (Zhang & Chen, 2003).
- Each phase and each component have their own set of distribution functions, meaning that memory demand and computing time increase significantly for multiphase simulations.
- The slope $\frac{\partial p}{\partial \rho}$ is lower in the liquid density region than it is in the vapour region, so the liquid is more compressible than the vapour (Sukop, 2006)
- The Maxwell construction of the SC-model gives the wrong vapour pressure (Sukop, 2006)
- $\Phi^k(x_\alpha)$ is not proportional to ρ which is why the surface tension is different to theory (He & Doolen, 2002)

2.6 Thermal Models

Cryogenic liquids tend to be at their saturation point at ambient conditions, because the best insulation cannot avoid heat being conducted into the liquid at the boundary condition, i.e. the tank wall. During start-up of rocket engines, the liquid may flow through pipes and manifolds not cooled down to or below the saturation point of the liquid, causing two phase flow. This short summary already explains the role the temperature plays in transient cryogenic two phas flow (TF) and why the isothermal multiphase models that exist for several years now (Shan & Chen, 1993), (Swift, et al., 1996), are not very suitable for describing this kind of problem. Since limitation to isothermal flows is a major drawback for any numerical scheme, in the past ten years a lot of effort has been put into the development of thermal models for the LBM.

There are many varieties of thermal models for the LBM. To the knowledge of the author, they all fall in one of the following categories

- the shifting approach
- the passive scalar approach
- the free energy model
- the multispeed approach

Sometimes it is not easy to distinguish between the models. One example of such a model is the one proposed in (Gonnella, et al., 2010). It is based on the free energy model and makes use of the passive scalar approach. Another example is the Shift model

presented in the next chapter. It also makes use of multiple speeds to increase numerical accuracy.

One problem that all these models have to deal with is the first order upwind scheme that the classical LBM equation 2.4 uses. The scheme is only accurate to the first order and therefore the time step needs to be small in order to keep the discretization errors small, too. To increase the stability and the usable range of the LBM, it is suggested to use a scheme of higher order instead (Sofonea & Sekerka, 2003), (Scagliarini, et al., 2010), (Gonnella, et al., 2007).

The following chapters will present the different models with a brief overview of what the underlying principles are and list their advantages and disadvantages.

2.6.1 The Temperature Shift Model

The Temperature Shift Model (TSM) uses a modification of the equilibrium distribution function f_{eq} to consider the temperature T (Sbragaglia, et al., 2009).

$$f^{eq}\left(\vec{\xi}, \rho, \mathrm{T}, \vec{\mathrm{u}}\right) = \frac{\rho}{(2\pi T)^{\frac{d}{2}}} \exp\left(-\frac{\left(\vec{\xi} - \vec{u}\right)^2}{2\mathrm{T}}\right) \tag{2.33}$$

This adds one equation to the relation between the distribution function and the macroscopic variables

$$\rho = \sum_a f_a \tag{2.34}$$

$$\rho\vec{u} = \sum_a f_a \vec{\xi}_a \tag{2.35}$$

$$d\rho T = \sum_a \left|\vec{\xi}_a - \vec{u}_a\right|^2 f_a \tag{2.36}$$

Another difference is the number of velocities used.

With this model (Sbragaglia, et al., 2009) recovers the correct Navier-Stokes-Fourier Equations

$$D_t = -\rho\partial_i \vec{u}_i^H \tag{2.37}$$

$$\rho D_t \vec{u}_i^H = -\partial_i p - \rho g \delta_{i,2} + \nu\partial_{jj}\vec{u}_i^H \tag{2.38}$$

$$\rho c_v D_t T^H + p\partial_i \vec{u}_i^H = k\partial_{ii} T^H \tag{2.39}$$

where superscripts H flag renormalized (physical) quantities, $D_t = \partial_t + \vec{u}_i^H \partial_j$ is the material derivative and viscous heating is neglected. c_v is the specific heat at constant volume for an ideal gas, ν is the viscosity and k the thermal conductivity. g is the gravity acceleration (Biferale, et al., 2012). See ref (Sbragaglia, et al., 2009) for a full description of the model.

The shifting approach implements energy conservation by introducing an additional suitable shift of the temperature field in the local equilibrium besides the momentum shift introduced by (Shan & Chen, 1993), (Gan, et al., 2012).

The classical LBM uses lattices like the D2Q9 for two dimensions or the D3Q19 for 3 dimensions. As explained in chapter 2.2 the first uses 9 velocities and the later 19 velocities for the possible directions the distribution function f can be streamed to. With this number of velocities, it is not possible to recover full Galilean invariance for the thermal model (Zhang & Chen, 2003). A space filling scheme in two dimensions would be D2Q37 and in three dimensions D3Q107 (Philippi, et al., 2006), (Surmas, et al., 2009), (He & Doolen, 2002).

The use of more velocities per node means that there is more data that needs to be stored. Compared to the classical LBM the multispeed model needs to store 5 times more variables per iteration step. The number of equations for the distribution function will increase accordingly and with it, the iteration time.

The Thermal Shift Model still suffers from spurious oscillations of temperature and spurious currents, so (Zhang & Chen, 2003) proposes to develop the LBM on a finite volume scheme of higher order. This work has been done for the classical LBM in (Scagliarini, et al., 2010).

The TSM looks promising from the thermodynamic viewpoint, but till now it only exists in a form that is able to describe ideal gases. However, the authors (Zhang & Chen, 2003) imply that it is not very complicated to expand it to real fluids. This step is necessary to simulate phase transitions with the model.

2.6.2 The Passive-Scalar Approach

In the passive-scalar approach (PS) the temperature is introduced into the LBM eq. 2.4 by a body force term acting on the fluid (Zhang & Chen, 2003). Using a body force term is a common way to take external effects into account in LBM. The way (Zhang & Chen, 2003) choose alters the collision term on the right-hand side of eq. 2.4 by adding a term

$$\Delta f_a(\vec{x}, t) = \frac{w_a}{T_0} \vec{\xi}_a \vec{F}(\vec{x}, t) \tag{2.40}$$

where w_a and T_0 are weights determined by the grid and $\vec{F}(\vec{x}, t)$ is the force acting on the particle distribution.

There are two other ways to do this. One is to modify the equilibrium distribution function, like it has been done in the TSM (Zhang & Chen, 2003). The other way supposes that the body force alters the macroscopic momentum and therefore the velocity $\vec{u}$. This new $\vec{u}$ then is used to calculate the equilibrium distribution function according to eq. 2.3 (Zhang, et al., 2004).

In the PS-model the temperature is not modified within the LBM equation itself. This is where the name of the model comes from. Instead the temperature gets changed by a supplemental scalar energy transport equation that is only dependent on macroscopic variables

$$\rho(\partial_t + \vec{u} \cdot \nabla)e = -p\nabla \cdot \vec{u} + \nabla \cdot \kappa \nabla T + \Psi. \qquad (2.41)$$

Here $e = c_v T$ is the internal energy, and c_v is the specific heat at constant volume. p is the pressure, κ is the heat conductivity. The term Ψ represents the viscous dissipation of flow and the contribution of surface tension (Zhang & Chen, 2003). Eq. 2.41 needs to be solved numerically with a suitable scheme.

The model is capable of simulating two phase flow with spontaneous phase transition, because it implements a van der Waals type Equation of State (EOS). There are several remaining issues that should be incorporated according to the author

- a more realistic EOS than van der Waals
- a more physical treatment of the heat capacity and latent heat
- further understanding and modelling of surface tension and near interface physics
- generalization of boundary conditions
- enhancement of numerical stability to achieve higher density ratios and lower viscosity

The last point is of special interest and one shortcoming of most multiphase models. One of the reasons for a lack in stability may be the first order finite difference scheme used for the classical LBM. However, in the PS model the first order finite difference scheme is not directly affecting the temperature and stability may be increased by using a higher order scheme to solve eq. 2.41.

Due to the coupling of the Temperature by a body force, the LB system and its equilibrium properties remain microscopically isothermal (Zhang & Chen, 2003). If this has an effect on numerical predictions and/or stability must be clarified in future research.

2.6.3 Free Energy or Mean Field Model

The so-called free energy model (FE) was first proposed by (Swift, et al., 1996). The model was inadequate for description of solid-fluid interactions (Zhang, et al., 2004) and the authors extended the FE model to the mean field model (MFM).

In the MFM the temperatures effect on the flow is considered by the force that alters the macroscopic velocity $\vec{u}$. This new $\vec{u}$ then is used to calculate the equilibrium distribution function according to eq. 2.3 (Zhang, et al., 2004).

$$\rho\vec{u} = \sum_a f_a\vec{\xi}_a + \tau\vec{F} \tag{2.42}$$

This force $\vec{F}$ is

$$\vec{F}(\vec{x},t) = -\nabla\overrightarrow{\Phi}(\vec{x},t) \tag{2.43}$$

where $\overrightarrow{\Phi}$ is a potential free energy field.

In order to obtain the NSE with a correct pressure term (Zhang, et al., 2004) uses an artificial term for $\overrightarrow{\Phi}$

$$\overrightarrow{\Phi}(\vec{x},t) = \rho(\vec{x})\psi'[\rho(\vec{x})] - \psi[\rho(\vec{x})] + \frac{1}{2}\rho(\vec{x})\int d\vec{x}'\phi_{ff}(\vec{x}'-\vec{x})[\rho(\vec{x}') - \rho(\vec{x})] - \frac{c^2(1-d_0)}{D}\rho(\vec{x}). \tag{2.44}$$

Here ψ and ψ' are the EOS for the neighbouring particles. (Zhang, et al., 2004) uses the van der Waals EOS and it approximates the potential $\vec{\phi}_{ff}$ to replace the integral term by a summation over its neighbours of a site $\vec{x}$.

$$\phi_{ff}(\vec{x}'-\vec{x}) = \begin{cases} K, & |\vec{x}'-\vec{x}| = c \\ 0, & |\vec{x}'-\vec{x}| \neq c \end{cases} \tag{2.45}$$

where c is a length in lattice units.

Apart from the model proposed by (Zhang, et al., 2004) there are others based on the free energy distribution by (Swift, et al., 1996), like the one by (Kalarakis, et al., 2002).

2.6.4 The Multispeed Model

The MSMs have been developed because the traditional D2Q7, D2Q9 and D3Q15. D3Q19, D3Q27 models are not able to correctly represent thermal and compressible flows that directly incorporate temperature in the equation for f_a^{eq} (He & Doolen, 2002).

Here we focus on a promising MSM introduced by (Watari & Tsutahara, 2003), which we call the WT Model.

2.6.4.1 The WT-Model for ideal gases

(Watari & Tsutahara, 2003) suggest a 2D thermal Finite Difference LBM (FDLBM) for which the Courant–Friedrichs–Lewy Condition $c = \Delta s/\Delta t$ is not equal to unity like it is for the classical LBM. This means that the velocities are independent of the lattice configuration. This way non-uniform grids, as well as mixtures with different masses can be used and because more enhanced numerical schemes are used to relate the velocities to the grid it improves numerical stability (Gonnella, et al., 2007).

The WT- model solves the Boltzmann equation with the Bathnagar, Kross and Grook collision term

$$\frac{\partial f}{\partial t} + \vec{\xi} \cdot \frac{\partial f}{\partial \vec{x}} = -\frac{1}{\tau}(f - f^{eq}) \tag{2.46}$$

where f is the particle distribution function, t is the time, $\vec{\xi}$ is the particle velocity vector, $\vec{x}$ the direction in Cartesian coordinates, τ the relaxation time and f^{eq} the equilibrium distribution function.

After a Chapman-Enskog Expansion (CEE), the WT model recovers the full set of the NSE with no errors (Watari & Tsutahara, 2003). Also, all observable fields like density, velocity and temperature are

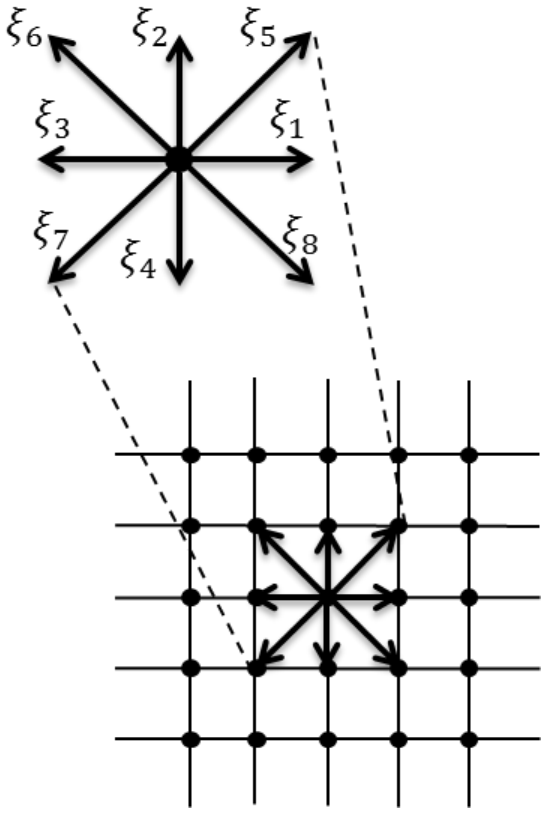

Figure 3. Quadratic grid for discretization.

derived from the same distribution function, as in standard kinetic theory (Sofonea, 2009).

This is achieved with a set of velocity vectors that ensures isotropy up to the seventh rank. The seventh rank isotropy is demanded by the set of first order velocity moments that are used in the derivation of the NSE and by the equilibrium distribution function. For the 2D model the velocity moments are

$$\sum_k \sum_{ki} f_{ki}^{(0)} = \rho \tag{2.47}$$

$$\sum_k \sum_{ki} f_{ki}^{(0)} \xi_{ki\alpha} = \rho u_\alpha \tag{2.48}$$

$$\sum_k \sum_i f_{ki}^{(0)} \xi_{ki\alpha} \xi_{ki\beta} = \rho\left(e\delta_{\alpha\beta} + u_\alpha u_\beta\right) \tag{2.49}$$

$$\begin{aligned} \sum_k \sum_{ki} f_{ki}^{(0)} \xi_{ki\alpha} \xi_{ki\beta} \xi_{ki\gamma} \\ = \rho\big[e\left(u_\alpha \delta_{\beta\gamma} + u\beta\delta_{\gamma\alpha} + u_\gamma \delta_{\alpha\beta}\right) \\ + u_\alpha u_\beta u_\gamma\big] \end{aligned} \tag{2.50}$$

$$\sum_k \sum_i f_{ki}^{(0)} \frac{c_k^2}{2} = \rho\left(e + \frac{u^2}{2}\right) \tag{2.51}$$

$$\sum_k \sum_i f_{ki}^{(0)} \frac{c_k^2}{2} \xi_{ki\alpha} = \rho u_\alpha \left(2e + \frac{u^2}{2}\right) \tag{2.52}$$

$$\begin{aligned} \sum_k \sum_{ki} f_{ki}^{(0)} \frac{c_k^2}{2} \xi_{ki\alpha} \xi_{ki\beta} \\ = \rho\left[e\left(2e + \frac{u^2}{2}\right)\delta_{\alpha\beta}\right. \\ \left. + u_\alpha u_\beta \left(3e + \frac{u^2}{2}\right)\right] \end{aligned} \tag{2.53}$$

The moments look familiar to the ones used in the derivation of the NSE for the classical LBM (see eq. 2.25), however they are adapted

to the higher number of velocity vectors and there are additional moments for taking thermal effects into account.

Because equation 2.53 contains the velocity u up to the fourth order the equilibrium distribution function f_{ki}^{eq} is derived to the fourth order, too

$$\begin{aligned} f_{ki}^{eq} = \rho F_k \Bigg[& \left(1 - \frac{u^2}{2e} + \frac{u^4}{8e^2}\right) + \frac{1}{e}\left(1 + \frac{u^2}{2e}\right)\xi_{ki\psi}u_\psi \\ & + \frac{1}{2e^2}\left(1 - \frac{u^2}{2e}\right)\xi_{ki\psi}\xi_{ki\eta}u_\psi u_\eta \\ & + \frac{1}{6e^3}\xi_{ki\psi}\xi_{ki\eta}\xi_{ki\zeta}u_\psi u_\eta u_\zeta \\ & + \frac{1}{24e^4}\xi_{ki\psi}\xi_{ki\eta}\xi_{ki\zeta}\xi_{ki\chi}u_\psi u_\eta u_\zeta u_\chi \Bigg]. \end{aligned} \tag{2.54}$$

In the WT-model there are 4 magnitudes of speeds in 8 directions plus a rest particle for a 2D simulation, which means that 33 distribution functions need to be solved (Watari & Tsutahara, 2003). For a 3D simulation there are 4 magnitudes of speeds in 32 directions plus one particle at rest, resulting in a total of 129 distribution functions that need to be solved for each node (Watari & Tsutahara, 2006), (Watari, 2007), (Watari, 2009).

The model uses a quadratic two-dimensional grid (see Figure 3), hence the components of the particle velocities are

$$\xi_{00} = 0, \xi_{ki} = \left[\frac{cos\,\pi(i-1)}{4}, \frac{sin\,\pi(i-1)}{4}\right] c_k, \tag{2.55}$$

where $i = 1, \dots, 8$ is the index for the direction and $k = 1, \dots, 4$ is the index for the set of absolute values of the velocity, c_k. The values for $c_k = [1.0, 1.92, 2.99, 4.49]$ were chosen by (Watari & Tsutahara, 2003) to increase the stability of the model. This leads to a total number of $\xi_{00} + \xi_{ki} = 33$ velocities.

The local values for the macroscopic density n, the velocity $\vec{u}$ and the temperature e are

$$n = \sum_{ki} f_{ki}, \tag{2.56}$$

$$nu_\alpha = \sum_{ki} f_{ki} \xi_{ki\alpha}, \tag{2.57}$$

$$n\left(e + \frac{\vec{u}^2}{2}\right) = \frac{1}{2} \sum_{ki} f_{ki} c_k^2. \tag{2.58}$$

e is the internal energy and relates to the temperature T by $e = RT$, with R being the specific gas constant.

The equilibrium distribution function has the form

$$f_{ki}^{eq} = nF_k s_{ki}, \tag{2.59}$$

with

$$
\begin{aligned}
s_{ki} = \left(1 - \frac{u^2}{2e} + \frac{u^4}{8e^2}\right) &+ \frac{1}{e}\left(1 - \frac{u^2}{2e}\right)\xi_{ki\psi}u_\psi \\
&+ \frac{1}{2e^2}\left(1 - \frac{u^2}{2e}\right)\xi_{ki\psi}\xi_{ki\eta}u_\psi u_\eta \\
&+ \frac{1}{6e^3}\xi_{ki\psi}\xi_{ki\eta}\xi_{ki\zeta}u_\psi u_\eta u_\zeta \\
&+ \frac{1}{24e^4}\xi_{ki\psi}\xi_{ki\eta}\xi_{ki\zeta}\xi_{ki\chi}u_\psi u_\eta u_\zeta u_\chi,
\end{aligned}
\tag{2.60}
$$

and the weights

$$
\begin{aligned}
F_k = \frac{1}{c_k^2\left(c_k^2 - c_{\{k+1\}}^2\right)\left(c_k^2 - c_{\{k+2\}}^2\right)\left(c_k^2 - c_{\{k+3\}}^2\right)} &\\
\times \Bigg[48e^4 &\\
+ 6\left(c_{\{k+1\}}^2 + c_{\{k+2\}}^2 + c_{\{k+3\}}^2\right)e^3 &\\
+ \left(c_{\{k+1\}}^2 c_{\{k+2\}}^2 + c_{\{k+2\}}^2 c_{\{k+3\}}^2\right. &\\
\left. + c_{\{k+3\}}^2 c_{\{k+1\}}^2\right)e^2 &\\
- \frac{c_{\{k+1\}}^2 c_{\{k+2\}}^2 c_{\{k+3\}}^2}{4}e\Bigg] &
\end{aligned}
\tag{2.61}
$$

$$F_0 = 1 - 8(F_1 + F_2 + F_3 + F_4).$$

The weights F_k follow the notation of (Sofonea, 2009). Please note that summation over repeated Greek indices (Einstein notation) is used in the equations above.

Since the speeds are not related to the lattice spacing, a finite difference scheme is used to discretize the model in space. We use the

flux limiter scheme based on the Lax-Wendroff scheme according to (Cristea, et al., 2006). Equation 2.46 then becomes

$$\frac{\partial f}{\partial t} = -\frac{c_k}{A_i \Delta s}\left[F_{ki}^{n,j+1/2} - F_{ki}^{n,j-1/2}\right] - \frac{1}{\tau}\left[f_{ki}^{n,j} - f_{ki}^{eq,n,j}\right], \quad (2.62)$$

where Δs is the lattice spacing, the superscript n indicates the current time step and j the node relative to the current node. A_i is a weighting factor. It is

$$A_i = \begin{cases} 1, & i \in \{1,\ 3,\ 5,\ 7\} \\ \sqrt{2}, & i \in \{2,\ 4,\ 6,\ 8\} \end{cases}. \quad (2.63)$$

The Fluxes $\mathcal{F}_{ki}^{n,j+1/2}$ and $\mathcal{F}_{ki}^{n,j-1/2}$ are

$$F_{ki}^{n,j+1/2} = f_{ki}^{n,j} + \frac{1}{2}\left(1 - \frac{c_k \Delta t}{A_i \Delta s}\right)\left[f_{ki}^{n,j+1} - f_{ki}^{n,j}\right]\Psi\left(\Theta_{ki}^{n,j}\right), \quad f_{ki}^{n,j} = f_{ki}\left(\vec{x}_j, t\right) \quad (2.64)$$

$$F_{ki}^{n,j-1/2} = F_{ki}^{n,(j-1)+\frac{1}{2}}.$$

where Ψ is the flux limiter and θ is the smoothness function

$$\Theta_{ki}^{n,j} = \frac{f_{ki}^{n,j} - f_{ki}^{n,j-1}}{f_{ki}^{n,j+1} - f_{ki}^{n,j}}. \quad (2.65)$$

The flux limiter proposed by (Cristea, et al., 2006) was not used, because we found the flux limiter by van-Leer to be more stable.

$$\Psi\left(\Theta_{ki}^{n,j}\right) = \begin{cases} 0, & \Theta_{ki}^{n,j} \leq 0 \\ \dfrac{2\Theta_{ki}^{n,j}}{\left(1+\Theta_{ki}^{n,j}\right)}, & 0 < \Theta_{ki}^{n,j} \end{cases} \tag{2.66}$$

(Watari & Tsutahara, 2003) showed that this discretization of equation 2.46 is equivalent to the following Navier-Stokes equations with no error after the Chapman-Enskog-Expansion has been applied:

$$\begin{aligned} &\frac{\partial \rho}{\partial t} + \frac{\partial}{\partial r_\alpha}(\rho u_\alpha) = 0 \\ &\frac{\partial}{\partial t}(\rho u_\alpha) + \frac{\partial}{\partial r_\beta}\left(\rho u_\alpha u_\beta + P\delta_{\alpha\beta}\right) \\ &\qquad - \frac{\partial}{\partial r_\beta}\left[\mu\left(\frac{\partial u_\beta}{\partial r_\alpha} + \frac{\partial u_\alpha}{\partial r_\beta} - \frac{\partial u_\gamma}{\partial r_\gamma}\delta_{\alpha\beta}\right)\right] = 0 \\ &\frac{\partial}{\partial t}\left[\rho\left(e + \frac{\vec{u}^2}{2}\right)\right] + \frac{\partial}{\partial r_\alpha}\left[\rho u_\alpha\left(e + \frac{\vec{u}^2}{2} + \frac{P}{\rho}\right)\right] \\ &\qquad - \frac{\partial}{\partial r_\alpha}\left[\kappa_e \frac{\partial e}{\partial r_\alpha}\right. \\ &\qquad \left. + \mu u_\beta\left(\frac{\partial u_\beta}{\partial r_\alpha} + \frac{\partial u_\alpha}{\partial r_\beta} - \frac{\partial u_\gamma}{\partial r_\gamma}\delta_{\alpha\beta}\right)\right] = 0. \end{aligned} \tag{2.67}$$

where P is the pressure, μ is the viscosity coefficient and κ_e is the heat conductivity. They are

$$P = \rho e, \tag{2.68}$$

$$\mu = \rho e \tau, \tag{2.69}$$

$$\kappa_e = 2\rho e\tau. \tag{2.70}$$

The WT model faces the same advantages and disadvantages like the TSM Model, because in order to increase numerical stability and accuracy the number of equations to be solved is also increased and hence numerical efficiency decreases. For 2D simulations the WT model has a slight advantage in comparison to the TSM model (33 to 37 distribution functions), but for 3D simulations it has a factor 6 of distribution functions to solve when compared to the classical LBM D3Q19, where the TSM "only" sees a factor of 5.

2.6.4.2 The WT-Model with Extension for Van der Waals Gases

The WT model itself is for ideal gases only (Gonnella, et al., 2007) and hence is not able to simulate phase transitions. At the same time it is not able to handle different Prandtl numbers for the same reason like all single relaxation LBM methods; the Prandtl number is fixed because the viscosity and the heat conductivity are both proportional to the relaxation time τ (Sofonea, 2009), (Alexander, et al., 1993).

One way around this limitation is the introduction of multiple relaxation time models (Alexander, et al., 1993). Another way is the one proposed in (Gonnella, et al., 2007). It introduces a force term I_{ki} which enables the WT model not only to do simulations with variable Prandtl number, but also enables it to simulate a van der Waals fluid. The force term I_{ki} represents the interparticle attraction forces. This way it is possible to simulate phase transition as a

continuous density change over the interface. In its discretised form eq. 2.71 then becomes

$$f_{ki}^{n+1,j} = f_{ki}^{n,j} - \frac{c_k \Delta t}{A_i \Delta s}\left[\mathcal{F}_{ki}^{n,j+1/2} - \mathcal{F}_{ki}^{n,j-1/2}\right] - \frac{\Delta t}{\tau}\left[f_{ki}^{n,j} - f_{ki}^{eq,n,j}\right] - \Delta t \cdot I_{ki}. \tag{2.71}$$

Since the Boltzmann equation is the microscopic description of a gas, the force term leads to a real gas which obeys the van der Waals (vdW) equation of state (EOS) for the Watari-Tsutahara-Gonella (WTG) -model.

The force term has the form

$$I_{ki} = -\big[A + B_\alpha(\xi_{ki\alpha} - u_\alpha) + \big(C + C_q\big)(\xi_{ki\alpha} - u_\alpha)^2\big] f_{ki}^{eq}\ ,\ eq.\ 5$$

$$A = -2\big(C + C_q\big)e\ ,\ eq.\ 12$$

$$B_\alpha = \frac{1}{ne}\big[\partial_\alpha(p^w - ne) + \partial_\beta \Lambda_{\alpha\beta} - \partial_\alpha\big(\zeta \partial_\gamma u_\gamma\big)\big]\ ,\ \ eq.\ 13$$

$$\begin{aligned} C = \frac{1}{2ne^2}\Bigg[& (p^w - ne)\partial_\gamma u_\gamma + \Lambda_{\alpha\beta}\partial_\alpha u_\beta - \big(\zeta \partial_\gamma u_\gamma\big)\partial_\alpha u_\alpha \\ & + \frac{9}{8} n^2 \partial_\gamma u_\gamma \\ & + K\Bigg(-\frac{1}{2}\big(\partial_\gamma n\big)\big(\partial_\gamma n\big)\big(\partial_\alpha u_\alpha\big) \\ & - n\big(\partial_\gamma n\big)\big(\partial_\gamma \partial_\alpha u_\alpha\big) \\ & - \big(\partial_\gamma n\big)\big(\partial_\gamma u_\alpha\big)\big(\partial_\alpha n\big)\Bigg)\Bigg] \end{aligned} \tag{2.72}$$

$$C_q = \frac{1}{2ne^2}\,\partial_\alpha[2qne(\partial_\alpha e)]$$

where

$$\begin{aligned} \Lambda_{\alpha\beta} = {} & M\partial_\alpha n \partial_\beta n - M\left(n\nabla^2 n + \frac{|\nabla n|^2}{2}\right)\delta_{\alpha\beta} \\ & - \left[ne\partial_\gamma n \partial_\gamma\left(\frac{M}{e}\right)\right]\delta_{\alpha\beta} \end{aligned} \tag{2.73}$$

is the contribution to the pressure tensor depending on the density gradients. $M = K + He$ allows a dependence of surface tension on

the temperature, ζ is the bulk viscosity, η is the shear viscosity and finally $p^w = 3ne/(3-n) - 9/8\, n^2$ is the vdW-pressure.

The WTG-model allows variation of the Prandtl Number

$$Pr = \eta/\kappa\_e \; = \tau/2(\tau - q) \tag{2.74}$$

through the variable q.

To calculate the derivatives, we used a nine-point stencil which is computationally efficient because it depends on the nearest neighbours, while on the other hand being fourth order accurate (Chung, 2002). This way the stability of the scheme was improved significantly.

The force term changes the heat conductivity k to $k = 2\rho T(\tau - q)$ and the Prandtl number to $Pr = \tau/2(\tau - q)$ so that when τ is fixed, q can be varied to change the Prandtl number (Gonnella, et al., 2007).

With the additional force term, it still is possible to obtain the correct NSE up to second order of Knudsen number without additional spurious terms (Gonnella, et al., 2007). It also allows to derive the NSE with all contributing stress terms. This includes surface tension as well as the full stress tensor including bulk and viscous stresses.

A shortcoming of being able to simulate real fluids with a variable Prandtl number is that the calculation time increases by 33% (Gonnella, et al., 2007) for the 2D model.

2.6.5 Temperature in classical LBM

A noteworthy way to incorporate a temperature into the LBM is by the one of (Yuan & Schäfer, 2006). The authors found a simple way to include different EOS directly into the LBM and by this way they solved stability issues limiting the density ratio between the phases. They were able to reach density ratios of up to 1000. However, there is no equation describing the evolution of temperature, which renders their model isothermal nonetheless.

3 Numerical work

From the comparison in section 2 it is clear that the multispeed models directly incorporate temperature in the LBM equations which is the most physical approach. They conserve Galilean invariance and have stability advantages because they rely on the use of higher order schemes to map the additional speeds to the lattice. For this reason, the model chosen for this work is the WT-model in conjunction with the Gonnella force term. The model will be called WTG from hereon.

3.1 Numerical Implementation

The classical LBM will be used to show the numerical implementation because it is straight forward and explains the principles specific to LBM.

Equation 3.1 and equation 3.2 for the equilibrium distribution function f_a^{eq} show that it is necessary to calculate the macroscopic variables ρ and u during each iteration.

$$f_a\left(\vec{x} + \vec{\xi}_a \Delta t, t + \Delta t\right) = f_a(\vec{x}, t) - \frac{\Delta t}{\tau}\left[f_a(\vec{x}, t) - f_a^{eq}(\vec{x}, t)\right] \tag{3.1}$$

$$f_a^{eq} = w_a \rho(\vec{x}) \left[1 + \frac{\vec{\xi} \cdot \vec{u}}{\chi c^2} + \frac{\left(\vec{\xi} \cdot \vec{u}\right)^2}{2\chi^2 c^4} - \frac{\vec{u}^2}{2\chi c^2}\right] \tag{3.2}$$

The steps for each iteration are summarized in Figure 4 (Begun & Basit, 2008). The actual steps where the LBM scheme gets iterated are the streaming step and the collision step. Streaming means that the old distribution function at the time $f_a(\vec{x}, t - \Delta t)$ gets forwarded to the next iteration step t in order to calculate the macroscopic variables and then the equilibrium distribution function out of it. At the collision step the collision term is used to iterate the new distribution function at the given time $f_a(\vec{x}, t)$.

The iteration scheme on the time derivative is the first order upwind scheme.

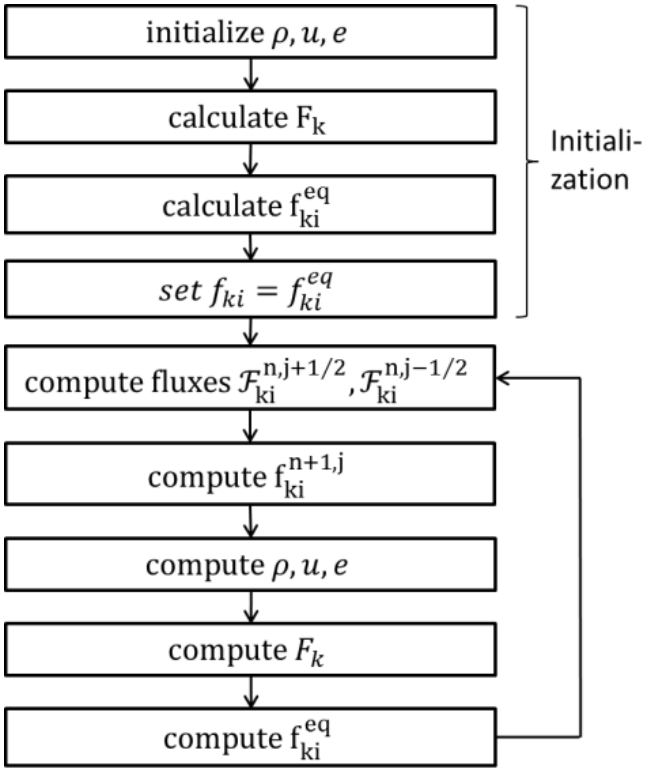

Figure 4: Iteration steps for the LBM

3.1.1 Boundary Conditions

There are several boundary conditions (BC) (Sukop, 2006), (Chung, 2002).

Periodic BC

Fluid that leaves the control volume on one side enters again on the opposite side.

Symmetric BC

The symmetric boundary condition reflects the flow distribution to the other side of the control volume, mirroring the flow. There is no flow across the boundary and no scalar flux across the boundary.

Bounce Back BC (BBBC)

A “particle” in the direction of the wall is temporarily stored and then re-emerges at the next time step with opposite sign. This way solid obstacles are defined in a simple way and no special programming treatment is necessary. Its simplicity makes it suitable even for complex geometries like porous materials. It is not perfect but the results obtained are good.

Constant Flux BC (von Neumann)

Density and Pressure are computed on the basis of conditions inside the domain and then they are used for computing the components of the distribution function at the boundary.

The Neumann BC (NBC) is implemented in the WTG model according to (Lou, et al., 2013).

Dirichlet BC

Arbitrary values at the BC are predefined.

Wall BC

The no-slip wall BC used in this work uses the diffuse reflection approach version 1 according to (Sofonea, 2009). It is comparable to the BBBC with the difference that the "particles" hitting the wall mix themselves in wall nodes, becoming Maxwellian, before being redirected into the fluid.

3.1.2 Wetting Parameter

Being able to adjust the contact angle of a bubble to a wall is important for evaporating bubbles at a heated surface (Mukherjee & Dhir, 2004) which is simulated as a validation case in section 3.2.2.

In its original form the WTG model is not able to wet surfaces correctly since no force term is implemented which represents the adhesion force of a liquid to a wall. In this work the force is implemented according to (Huang, et al., 2015) as an additional term on the right-hand side

$$f_{ki}^{n+1,j} = f_{ki}^{n,j} - \frac{c_k \Delta t}{A_i \Delta s}\left[\mathcal{F}_{ki}^{n,j+1/2} - \mathcal{F}_{ki}^{n,j-1/2}\right] - \frac{\Delta t}{\tau}\left[f_{ki}^{n,j} - f_{ki}^{eq,n,j}\right] - \Delta t \cdot (I_{ki} + I_{ki} \cdot w_p). \tag{3.3}$$

The term $I_{ki} \cdot w_p$ is an attractive force which is only applied to the nodes closest to the wall. The magnitude of the force is controlled by the wetting parameter w_p and this way the contact angle of the liquid gas interphase can be adjusted to the physical values.

To adjust w_p a single liquid droplet was simulated which was initi-

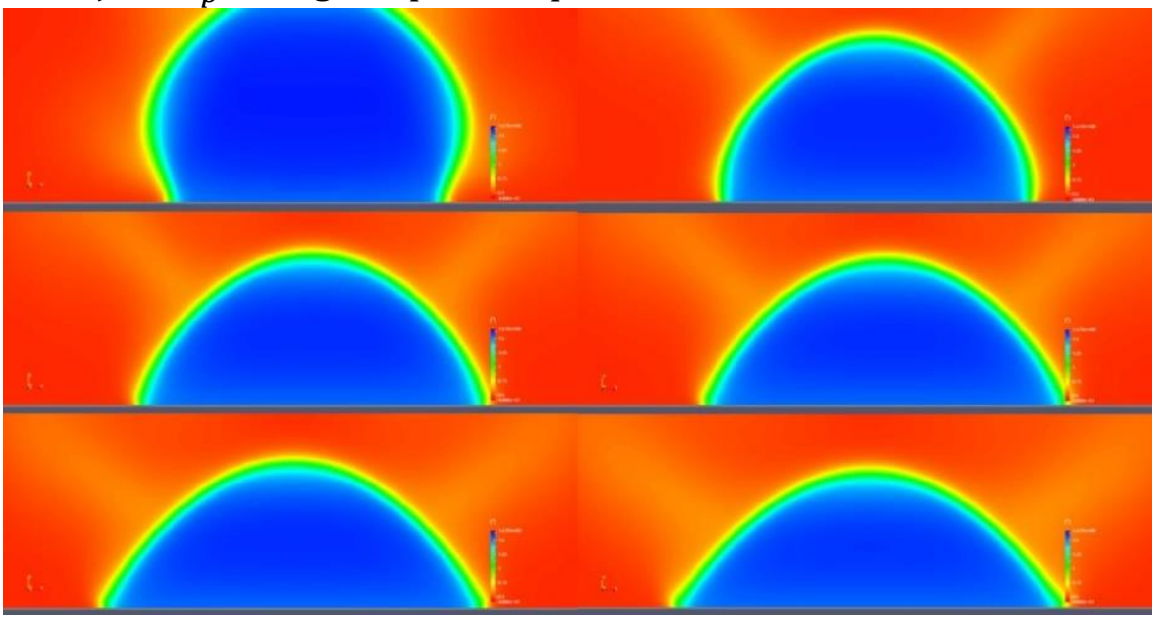

Figure 5: Liquid droplet at a wall in thermodynamic equilibrium for a wetting parameter range of $-0.7 < w_p < -1.1$

ated close to the wall. After the droplet fell on the bottom wall and reached thermodynamic equilibrium the contact angle of the droplet at rest was measured. The wetting parameter was varied from $-0.7 < w_p < -1.1$ in six steps as shown in Figure 5 and the corresponding angles are

Table 1. LOX contact angles at the wall

Wetting parameter, w_p	**Contact angle, θ**
-0.7	115°
-0.8	101°
-0.9	65°
-0.95	57°
-1.0	54°
-1.1	50°

The simulation was set up for liquid oxygen (LOX) at 139K saturation temperature and 12 bar saturation pressure on a 512 x 512 grid. The simulation and experiments by (Mukherjee & Dhir, 2004) for water were used since there is no contact angle data available for LOX to the knowledge of the author. The relations given by (Mukherjee & Dhir, 2004) were used to transfer the parameters governing the experiment to LOX. The LOX drop was initiated with a radius of $r_{bubble} = 0.07mm$ discretized by 60 nodes. Non-slip wall boundary conditions were used on all walls.

The Morton number Mo was used to set up the LBM. The Morton number describes the similarity of bubbles which are rising in a liquid (Pfister & Hager, 2014) and is given by

$$Mo_{LOX} = Mo_{LBM} = \frac{g\eta_L^4 \Delta\rho}{\rho_L^2 \sigma^3} = 4.78 \cdot 10^{-11}. \qquad (3.4)$$

The Morton number is defined by the gravity $g = 9.81 m/s^2$, the viscosity of the liquid $\eta_L = 84{,}3\mu Pas$, the density difference of liquid and gas $\Delta\rho = 597 kg/m^3$, the density of the liquid $\rho_L = 723 kg/m^3$ and the surface tension $\sigma = 2{,}3 mN/m$.

Since the contact angle is dependent on the surface microstructure, contamination and other factors it is difficult to measure (Brennen, 2005) and no literature on it could be found for LOX. For this reason, the arbitrary choice was made to use a $\theta = 54°$ as found in the experiments by (Mukherjee & Dhir, 2004) for water. This is to be considered as a starting point for the LOX simulations and should be addressed in future work to increase the accuracy of the simulation.

3.1.3 Setting up a simulation

The LBM uses the equations of statistical thermodynamics. These have been developed to explain the equations of continuum thermodynamics which are well known. Statistical thermodynamics explains the nature of gases and liquids from a microscopic point of view, by describing the motion of atoms or molecules. The LBM is the discretized version of these equations, which means that they don't describe the evolution of the motion of molecules but of a direction specific density. By doing so, the LBM creates a kind of its

own gas or liquid, which is seen by the specific gas constant R being equal to 1.

Due to this nature the simulation done by the LBM is always a simulation of the liquid which is described by the discretized Boltzmann equations. As such it is its own liquid and not a physical liquid like water or liquid oxygen. This means, if one wants to simulate liquids which are different from the LBM liquid, one has to use similarity laws and numbers to transfer the LBM results to the desired fluid.

For fluid properties, like the density ρ, pressure p and temperature e this is done with the corresponding states principle (CSP). The CSP has been discovered by the vdW-EOS and states that every fluid has the approximately the same compressibility factor $Z_c = 1$ at the critical point.

This means the physical properties are made dimensionless by the following expressions (Watari & Tsutahara, 2003).

Density:	$\rho, f_{ki}, f_{ki}^{eq}$	by ρ_c
Speed:	c_{ki}, u_α	by $\sqrt{R_s T_c}$
Energy:	e	by R_s, T_c
Temperature:	T	by T_c
Coordinate:	r_α	by L
Time:	t, τ	by $\frac{L}{\sqrt{R_s T_c}}$
Pressure:	p	by p_c *or* $\rho_c R_s T_c$
Diffusion	μ, k	by $\rho_c L \sqrt{R_s T_c}$

Where the index c indicates critical values, μ is the dynamic viscosity, k the heat conductivity.

This leads to the following equations for deriving LBM properties for the ideal gas WT-model. The superscript * indicates LBM properties

$$
\begin{aligned}
T^* &= \frac{T}{T_c} \\
e^* &= \frac{R_s T}{R_s T_c} = T^* \\
c^* &= \frac{\sqrt{\kappa R_s T}}{\sqrt{R_s T_c}} = \sqrt{\kappa T^*} \\
\kappa^* &= \frac{f+2}{f} = 2\,, \quad (2D \rightarrow f = 2) \\
p^* &= \frac{\rho R_s T}{\rho_c R_s T_c} = \frac{p}{p_c} \\
\mu^* &= \frac{\rho e \tau}{\rho_c L \sqrt{R_s T_c}} \\
\sigma^* &= \frac{\sigma}{L p_c} \\
g^* &= \frac{gL}{R_s T_c} \\
k^* &= \frac{2\rho e \tau}{\rho_c L \sqrt{R_s T_c}} \\
ds^* &= \frac{L}{N_x}
\end{aligned}
\tag{3.5}
$$

Other parameters are chosen according to the problem under investigation, as was shown in section 3.1.2 and as will be shown by the simulation of the validation cases. Examples are the Reynolds-number, the Morton-number or the Prandtl-number.

It is obvious, that balancing all of the similarity laws in a way that the simulation represents the real fluid becomes more and more difficult the more parameters of influence there are, like

temperature or different phases. But the biggest drawback is that the CSP is only accurate for single atomic gases (Xiang, 2005) which are the noble gases basically and it deviates more and more the more asymmetric the fluid molecules become. This means that the LBM is acceptable for two atomic fluids like liquid nitrogen or liquid oxygen, but results will get worse for small but highly polar molecules like water and will be very likely not acceptable for fluids with large molecules like petrol or kerosene.

3.2 Validation Cases

As mentioned in the introduction (sec. 1) a numerical code used for rocket engine applications needs to be able to simulate thermal two-phase flow and cavitation, wall heat transfer, complex geometries and also compressible flow. The code also has to be stable around the thermodynamic critical point since the fluids are subcritical when they come from the tank and it is possible that they are supercritical after being pressurized in the turbopump and heated up in the cooling channels.

To verify whether the model is capable of simulating the points mentioned above, a validation logic with simplified test cases was set up. Four test cases were chosen:

1. lid driven cavity
2. single vapour bubble at heated surface
3. Riemann shock tube

4. cryogenic water hammer

Overall correct representation of incompressible single-phase flow will be demonstrated by a lid driven cavity. Instantaneous evaporation will be simulated by the formation of a single vapour bubble at a heated surface. The Riemann shock tube configuration will show the capability of the model to handle shocks and supersonic flow. The final validation test case will be the simulation of water hammer in liquid nitrogen.

3.2.1 Driven Cavity

The Driven Cavity is a validation case in NASAs "NPARC Alliance Verification and Validation Archive". It is a validation case to prove laminar incompressible flow at various Reynolds numbers[10].

The driven cavity is a box with closed walls on three sides and one wall with a constant velocity BC at the top. At the left, bottom and right wall we used the diffuse reflection BC (see section 3.1.1). The simulation was performed with the ideal gas model. The gas in the computation is nitrogen with a temperature of 114 K at a pressure of 0.306 MPa.

The computational domain was 256x256 for all cases. A simulation with 512x512 nodes did not show an improvement so grid convergence is assumed.

The driven cavity was simulated for three Reynolds numbers 400, 1000, 5000 and the streamline contours are compared to the results from (Ghia, et al., 1982) in Figure 6. The results are in good

agreement. For Re=400 and Re = 5000 there are some deviations in the main vortex position, while it is in perfect agreement for Re = 1000. The lower left vortex is slightly smaller for Re = 400 and Re = 1000, while it is exactly the same size for Re = 5000. For the latter there is a deviation in the lower right vortex. The additional vortex in the results for Re = 5000 at the top left is simulated very well.

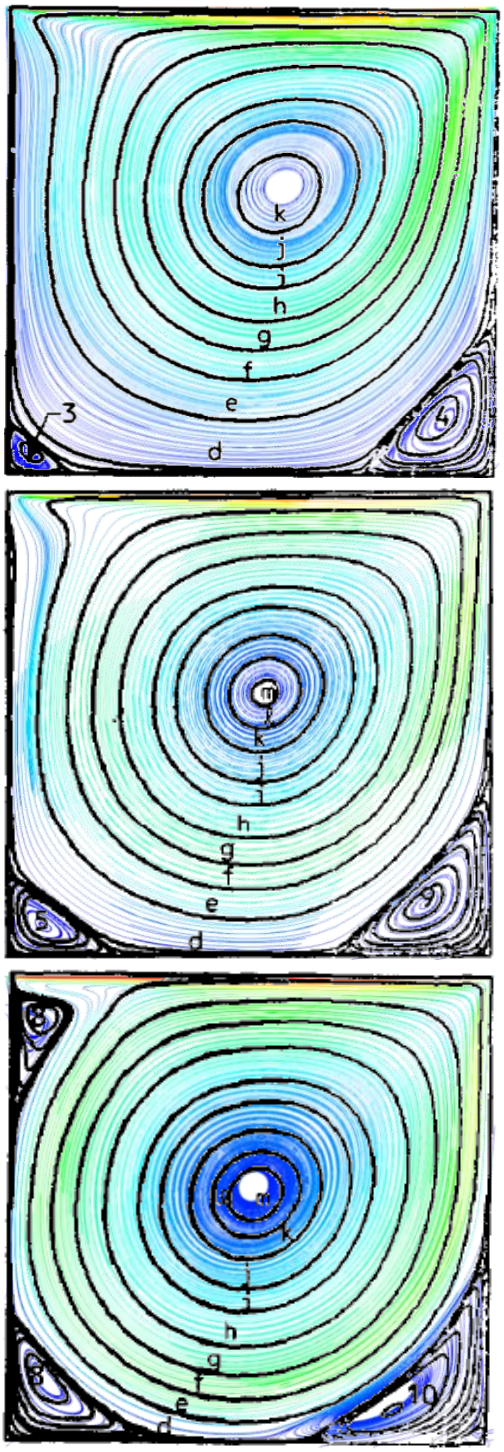

Figure 6: Driven cavity, streamlines for Re = 400, 1000 and 5000 (coloured, top to bottom), (Ghia, et al., 1982)(black).

3.2.2 Saturated film boiling

To test the real gas WTG-model we set up a simulation in a rectangular simulation domain of 200x600 nodes. The BC at the top wall is a Neumann Outflow BC (see section 3.1.1), at the left and right

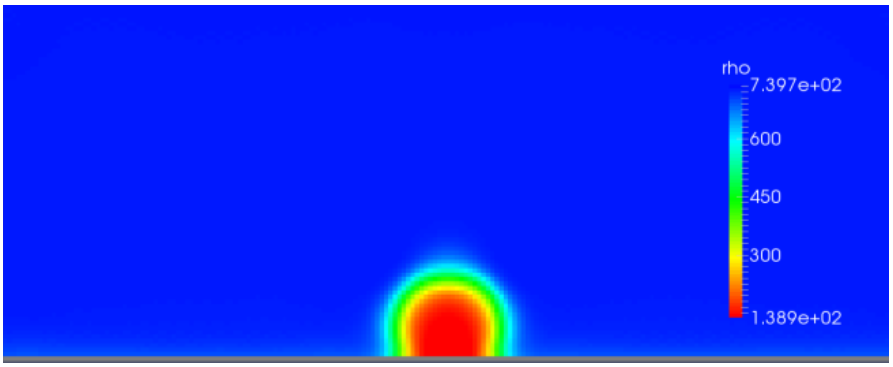

Figure 7: Evolution of oxygen bubble at time t = 14ms.

wall there is a periodic BC and at the bottom the diffuse reflection BC. The simulated fluid is liquid oxygen with an initial bulk temperature of 139 K, which is the saturation temperature at the density of 723 kg/m^3 and the pressure of 12 bar. The whole computational domain is filled with fluid initially. The bottom wall is set up with a temperature of 144 K everywhere except for a 5-mm wide area in the middle which is initialized to a temperature of 201 K. This way spontaneous saturated film boiling at a superheated wall is simulated (see Figure 7).

Figure 7 shows the evolution of the gas bubble after 14 ms. The simulation shows the ability of the model to handle evaporation at the wall. The temperature profile inside the bubble shows a linear

distribution (see Figure 8). The linear distribution is confirmed by the measurements of Ref. 13).

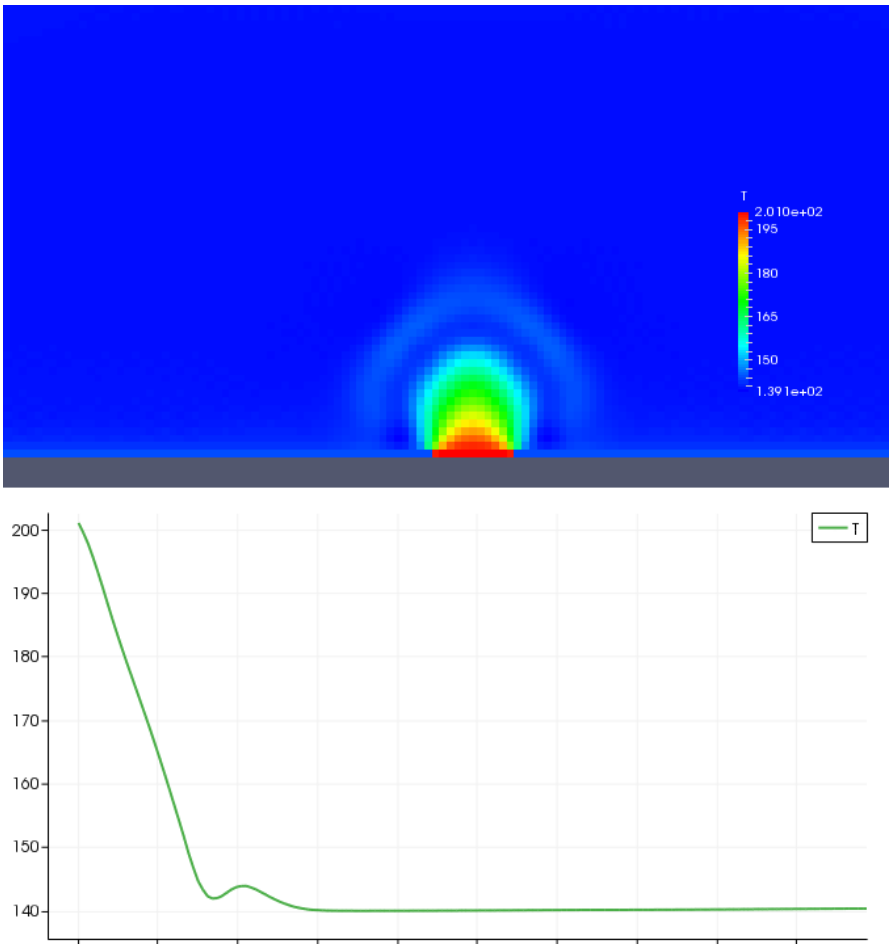

Figure 8: 2D temperature distribution at the bubble at time t = 14ms (top), cut through the middle of the bubble (bottom).

3.2.3 Riemann shock tube

In Ref. 5) Watari and Tsutahara used the WT-model to simulate the ideal compressible flow in a nozzle. With their work the authors showed that the scheme is able to simulate choked flows. Since they did not go into detail on the shock formation in the flow, we decided

to investigate this phenomenon by simulating a typical Riemann shock tube configuration.

In the Riemann shock tube there is gas in two compartments separated by a diaphragm. By setting the pressure in one compartment higher than in the other a shock is generated at the contact plane as soon as the diaphragm is removed. There are analytical solutions for the shock tube to which the simulation has been be compared. Like the driven cavity simulation the shock tube is also part of in NASAs "NPARC Alliance Verification and Validation Archive" (Slater, 2015).

Table 2. initial values for shock tube simulation

Simulation	**Temp. T_1, T_2**	**density,n_1**	**density,n_2**
ST1	139 K	43.6 kg/m^3	87 kg/m^3
ST2	139 K	43.6 kg/m^3	109 kg/m^3
ST3	139 K	43.6 kg/m^3	131 kg/m^3
ST4	170 K	43.6 kg/m^3	170 kg/m^3

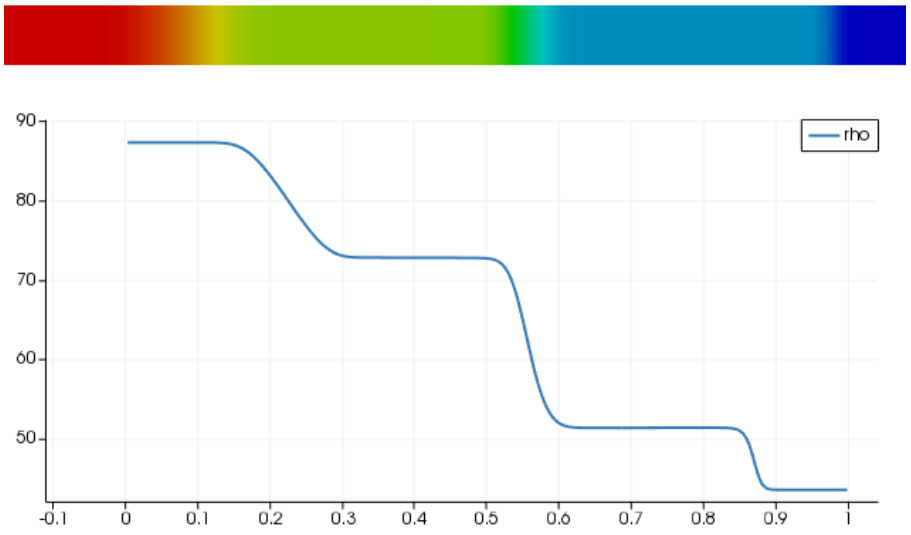

Figure 10: Computational domain (top), density plot over the middle line of the same domain (bottom) at time t = 1,197ms.

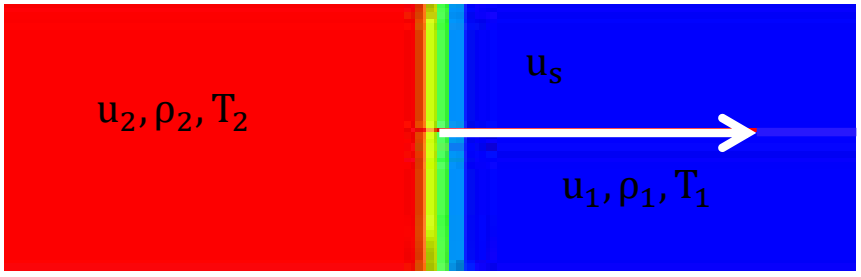

Figure 9: notation before and after the shock.

All shock tube simulations are done for oxygen with the ideal gas model. The density in the right half n_1 is kept constant at 43.6 kg/s while the temperature T_1 and the properties in the right half of the shock tube are varied in order to check the validity of the model's predictions. The parameter matrix for the simulations is summarized in Table 2.

All simulations are done on a 512x32 grid. To study grid convergence a simulation on a 1024x64 grid was performed but did not show a shift in the results. The BCs on the left and right wall are diffuse reflection BCs while the top and lower BC is periodic.

Figure 10 shows the computational domain as well as the density on the centre-line. One clearly sees that, although the scheme is not optimised for numerically simulating supersonic flow, it has no problem in capturing all relevant fluid dynamic effects which are the shock, the contact discontinuity and the expansion wave. The scheme simulates the shock and the contact discontinuity as a continuous change in density with a gradient which is too low (Wagner, 2005), but nevertheless the values after the shock are in very good agreement with the analytical solution as we will show now.

The analytical solution of the velocity after the shock u_2 is according to (Wagner, 2005)

$$u_2 = \frac{c_2 \cdot (Ma_s^2 - 1)}{\left[\left(1 + \frac{\kappa - 1}{2} Ma_s^2\right)\left(\kappa Ma_s^2 - \frac{\kappa - 1}{2}\right)\right]^{0.5}} \tag{3.6}$$

where $c_2 = \sqrt{\kappa R T_2}$ is the speed of sound after the shock and Ma_s is the velocity of the shock. The pressure is

$$p_2 = \frac{2}{\kappa + 1}\left(\kappa Ma_s^2 - \frac{\kappa - 1}{2}\right) \tag{3.7}$$

and the temperature

$$T_2 = T_1 \cdot \left(\frac{2}{\kappa+1}\right)^2 \frac{1}{Ma_s^2}\left(1+\frac{\kappa-1}{2}Ma_s^2\right)\left(\kappa Ma_s^2 - \frac{(\kappa-1)}{2}\right). \tag{3.8}$$

In the equations above the indices were chosen according to Figure 9.

Table 3. Deviation of simulation values from analytical values

	$\%\boldsymbol{u_2}$	$\%\boldsymbol{p_2}$	$\%\boldsymbol{T_2}$	$\%\boldsymbol{n_2}$	$\boldsymbol{Ma_s}[-]$
ST1	0.17	0.06	0.04	0.02	1.138
ST2	0.96	0.44	0.21	0.23	1.188
ST3	0.28	0.14	0.08	0.07	1.226
ST4	0.32	0.12	0.05	0.07	1.139

To determine the Mach number of the shock $Ma_s = u_s/c_1$ the speed u_s is read from the results. Together with the known values T_1 and p_1 the properties after the shock are calculated and then compared to the values from the simulation. Table 3 shows that the simulation error is less than 1% in all cases.

3.2.4 Water hammer in liquid nitrogen

Pressure surge is of strong interest in many industrial fields, amongst which the space industry. In rocket engines and thrusters, it plays a major role in the designing process of the feed system and has to be considered especially when the feed lines are primed during start-up as well as during the rapid closing of valves upon shutdown. In both cases a pressure peak occurs, leading to a pressure surge wave travelling along the pipe.

Pressure surge is a well-studied phenomenon because of its importance for the designer of fluid systems. For CFD tools it is a valuable validation experiment to check whether the code is able to correctly simulate steep pressure gradients, absolute pressure peaks and wave attenuation. When the pressure falls below the saturation pressure, the complexity of the flow simulation increases significantly because of instantaneous evaporation and condensation.

Due to the importance for rocket engines it is investigated how the WTG model is able to simulate pressure surge events. Three simulations have been performed with liquid nitrogen (LN2) in order to show the above:

- **Pressure Surge in a straight conduct;** to show the overall behaviour of the LBM for this case
- **Pressure Surge with a single bubble;** to show the wave propagation over a single nitrogen vapour bubble

- **Pressure Surge with 25 bubbles;** to show the wave propagation through a duct completely obstructed by bubbles

3.2.4.1 Numerical setup

$M = K + He$ allows a dependence of surface tension on the temperature e but in all simulations, H was set to 0 and K was set to 0.005. This value has been chosen mainly to improve numerical stability and to counter bubble deformation by spurious currents at the interface. The latter are a common problem of multiphase codes in general, not only LBMs (Chung, 2002).

ζ is the bulk viscosity, η is the shear viscosity and finally $p^w = 3ne/(3-n) - 9/8\, n^2$ is the vdW-pressure.

The WTG-model allows variation of the Prandtl number $Pr = \eta/\kappa\_e = \tau/2(\tau - q)$ through the variable q.

3.2.4.2 Boundary and initial conditions

There are two types of boundary conditions (BC) which we use in this paper. A Dirichlet BC is implemented to fix values at the wall, like the velocity for example for which a no-slip wall-BC is used based on the diffuse reflection BC version 1 in (Sofonea, 2009).

The left wall and the bulk volume are set up with an initial velocity in the positive direction of $u_0 = 5.87\, m/s$, which represents a steady flow before the computation starts.

The fluid velocity at the right wall is “0” at all time. This way a “valve” with an infinite closing speed is simulated and a pressure surge will evolve from the right wall.

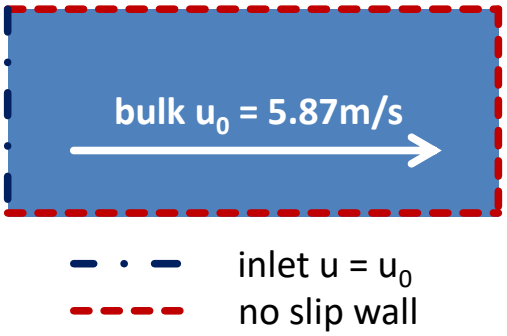

Figure 11: Boundary conditions

The thermodynamic properties of each of the following simulations are found in the respective chapters.

3.2.4.3 Numerical setup and results

Three simulations are chosen to show how nitrogen behaves in a pressure surge event. All of the 2D simulations use the same rectangular computation area with a height of 19 mm and a length of 76 mm. The height represents the same inner diameter of the pipe used in (Traudt, et al., 2015). Since this work focusses on first few milliseconds of the interaction of a pressure surge with vapour bubbles formed by cavitation, the length has no impact on the wave propagation, i.e. the simulation did not run long enough to lead to a reflection of the pressure wave on the “left” wall.

First a simulation of a pressure surge event with no vapour bubbles is performed. Then a single bubble is introduced in the duct to show how the incoming pressure wave is reflected at the bubble surface and how the pressure evolution in the bubble is. The last simulation presented in this work is set up with bubbles everywhere, so that the pressure wave cannot travel in the negative direction without impacting on a phase interface, i.e. there is no free path for the pressure wave in the rectangular duct.

In all simulations the bubble size is set to 26 nodes (4.9 mm) as a proof of concept.

The natural frequency of a nitrogen bubble of this size has been calculated to 62.5 kHz (according to (Leighton, 1994)) which equals a period of 16 μs. This value is at least an order of magnitude lower than the time scale of the pressure waves simulated in this paper.

The boundary conditions are the same for all three simulations (see section 3.2.4.2).

All simulations use the real gas model, even if there is only a single phase.

3.2.4.3.1 Single phase pressure surge

The single-phase simulation was set up with the properties for LN2 summarized in Table 4. The properties are for the van der Waals

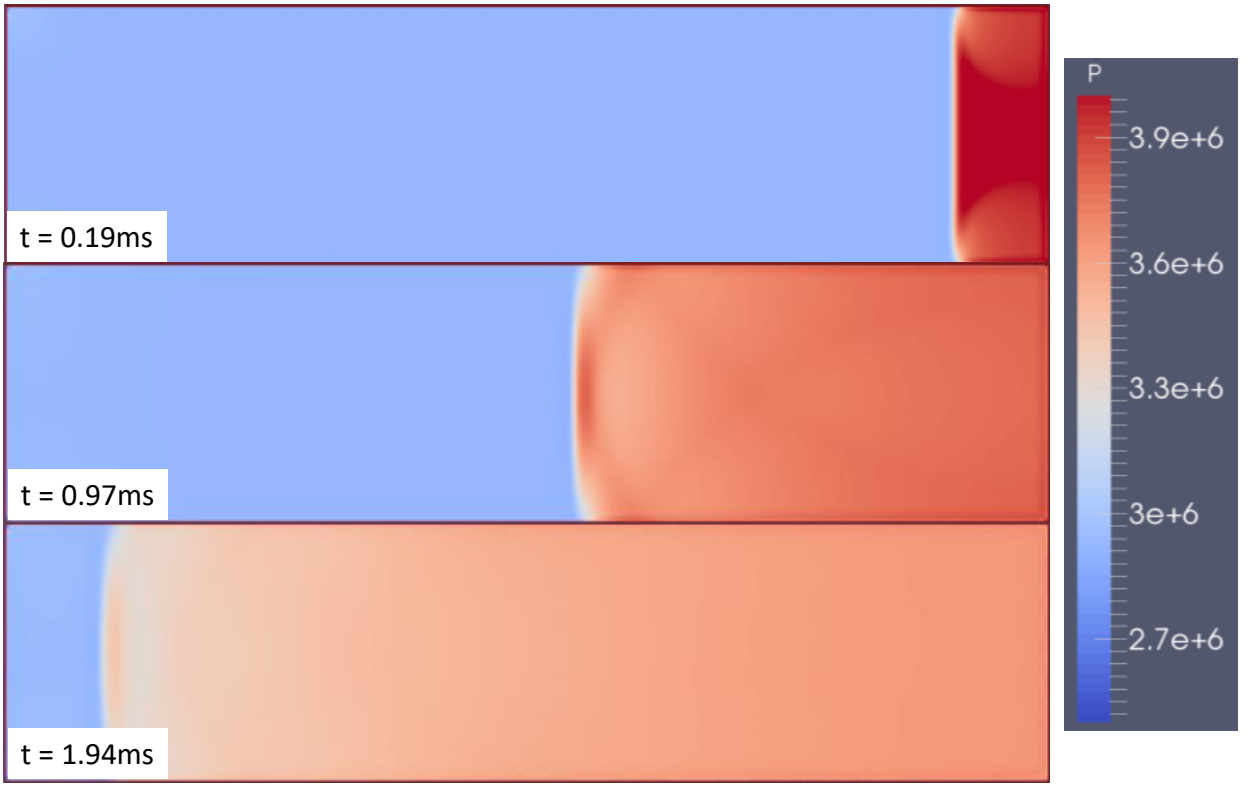

Figure 12: Single phase pressure surge simulation

(vdW) fluid which is simulated by the WTG model and since the vdW EOS is known to be not very accurate, they are slightly different from the real fluid properties. For this reason, the third column in Table 4 shows the real fluid properties of the NIST (National Institute of Standards and Technology, 2018) for LN2 at the temperature of 116 K.

Table 4: Fluid properties for single phase pressure surge initialization

Property	LBM	NIST	
density ρ	519	586	kg/m^3
temperature T	116	116	K
pressure p	2.91	2.91	MPa
nodes Nx	512		
nodes Ny	128		

The results are shown in Figure 12. It is obvious that the WTG model has some disadvantages for simulating pressure surge. One can easily see that the dissipation of pressure is relatively high. The pressure decreases from the top picture to the bottom picture from 4.05 MPa, over 3.77 MPa to 3.63 MPa. At t = 0.19 ms low pressure evolving from the wall reduces the main surge pressure. Apparently, the boundary conditions are causing some of the dissipation while the numerical model itself seems to have some inherent numerical damping, too. This is also seen in the surge pressure in the simulation, which is below the Joukowsky pressure $p_0 + \Delta p = p_0 + \rho c u_0 = 4.36$ MPa. Here p_0 is the mean pressure before the pressure surge event.

Apart from that, the speed of sound is predicted well within the limits of the vdW EOS. From the distance the wave travelled and the time needed for it, a value of 473 m/s is calculated. The fluid is close to the critical point and for this reason has a relatively high sensitivity to the actual values of temperature and pressure. Depending on the pressure the speed of sound varies from 420 m/s for 2.91 MPa to 466 m/s for 4.05 MPa (National Institute of Standards and Technology, 2018) where the latter is the pressure behind the pressure wave.

3.2.4.3.2 Single bubble pressure surge

The single bubble simulation is set up on the same rectangular grid with the same temperature, pressure and liquid density as the single-phase simulation. The properties are summarized in Table 5. The properties are the saturation properties for the vdW EOS.

Table 5: fluid properties for single bubble pressure surge initialization

density liquid ρ_l	519	kg/m^3
density vapor ρ_v	133	kg/m^3
temperature T	116	K
pressure p	2.91	MPa
nodes Nx	512	
nodes Ny	128	

The bubble and the liquid have the initial velocity of $u_0 = 5.87\ m/s$. The position of the bubble is at node 400 in x-direction and in the middle of the duct in y-direction. The radius of the bubble is 13 nodes (4.9 mm in diameter).

The main reason for the simulation with a single bubble is to show the pressure wave bubble interaction in a simple example. The same structures will also be visible in the simulation with more bubbles, but they will not be so easy to distinguish because they are as numerous as the number of bubbles in the simulation.

Figure 13 shows the results of the simulation. The first two pictures show a low-pressure wave which originates from the bubble, as well as the pressure surge coming from the right wall. The small wave coming from the bubble is due to non-equilibrium initialization.

In the third picture at time t = 0.485 ms the main pressure wave passes the bubble. There are three effects visible.

The first one is the reflection of the pressure wave at the bubble interface as a negative pressure wave.

The second effect visible is how each contact point of the main pressure wave with the interface starts a pressure wave inside the bubble, which itself travels with the lower speed of sound in the vapour in the bubble. This can also be tracked in the fourth picture. For our experiments the density ratio is 3.9 which is very close to the numerical simulation presented in (Giordano & Burtschell, 2006) where a bubble of Krypton gas in air has been simulated (density

ratio of 2.9). Since Krypton has a lower SOS than air the results show a comparable behaviour of the pressure distribution in the bubble. The authors validated their simulations against experimental results and achieved very good agreement (Giordano & Burtschell, 2006).

The third effect visible in the third picture is the low-pressure wave mentioned before which has its origin in non-equilibrium initialization. It leads to a distortion of the bubble. It is no longer round in shape, but more a square. This effect is pronounced by spurious currents at the interface. Spurious currents at phase interfaces are a known problem in numerical codes (Yuan & Schäfer, 2006), (Chung, 2002). A test simulation done with a bubble without external disturbances did not show this behaviour.

In Figure 13 the pictures from 0.573 ms to 0.776 ms show that after the pressure wave inside of the bubble “collapses” or reunites at the front of the bubble, a new pressure wave is sent off from the front of the bubble which travels behind the main pressure wave of the pressure surge event. This behaviour has also been observed by (Giordano & Burtschell, 2006). Moreover, Figure 13 shows a maximum of the pressure inside the bubble at t = 0.776 ms.

There is no “bubble collapse” visible. Past experiments with water showed (Traudt, et al., 2015) that the collapse time of a bubble is in the order of 6ms. The same behaviour of LN2 gas bubbles is expected as the ones observed in water. The simulation deviates here from the experimental observation. The “bubble collapse” is driven

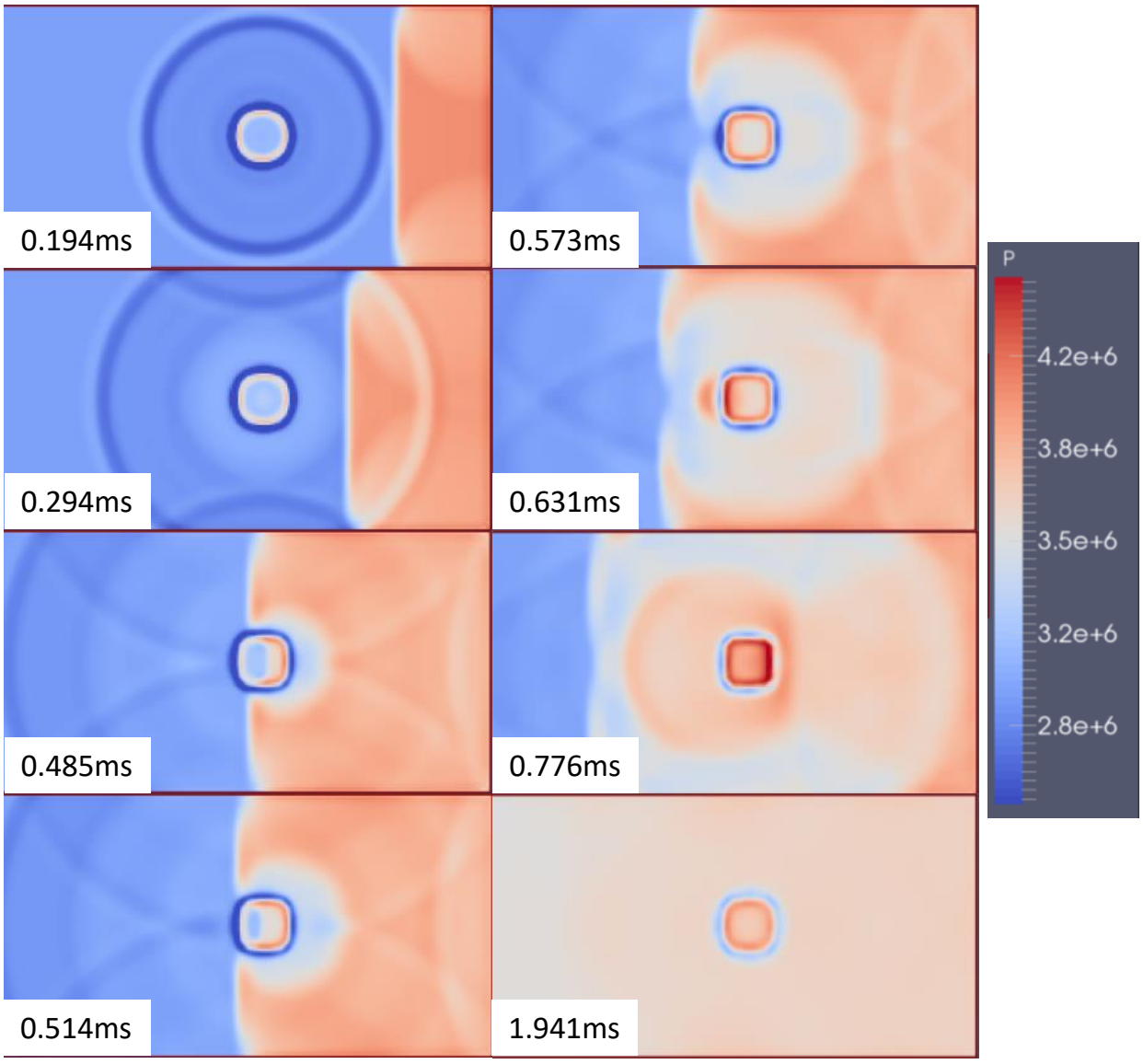

Figure 13: Single bubble pressure surge simulation

the so called Richtmyer-Meshkov instabability formed at the interface between two fluids with different densities. This instability is of small scale and cannot be resolved in the numerical simulations presented in this paper. The resolution of the mesh on the initial bubble diameter is 0.19 mm. In (Giordano & Burtschell, 2006) the

authors were not able to reproduce the instabilities with a resolution of 0.1mm.

3.2.4.3.3 Multiple bubble pressure surge

25 circular bubbles were positioned in equal distance from each other for this simulation. This way the pressure wave cannot travel upstream without passing a liquid vapour interface. The bubbles all have a diameter of 13 nodes as in the previous simulation and a distance of 52 nodes from each other. The fluid properties are the same as for the simulation with a single bubble. The results are shown in Figure 14 and Figure 15.

Till time t = 0.776 ms the behaviour of the pressure wave is comparable to the single bubble case. At time t = 0.97 ms there is no pressure wave front visible anymore in between the bubbles, but the pressure inside of the bubbles is a good indication on where the pressure surge is at the moment. After 1.941 ms it is obvious that the speed of sound is lower than in the single-phase case of the first simulation presented in this paper (284 m/s).

There is strong attenuation of the pressure wave. One has to keep in mind that the model in use shows numerical dissipation of pressure (see section 3.2.4.3.1), but nevertheless it is obvious that diffraction and reflection of the pressure wave at the phase interface also play an important role in wave propagation and attenuation.

As in the single bubble case “bubble collapse” is not visible, which is unexpected.

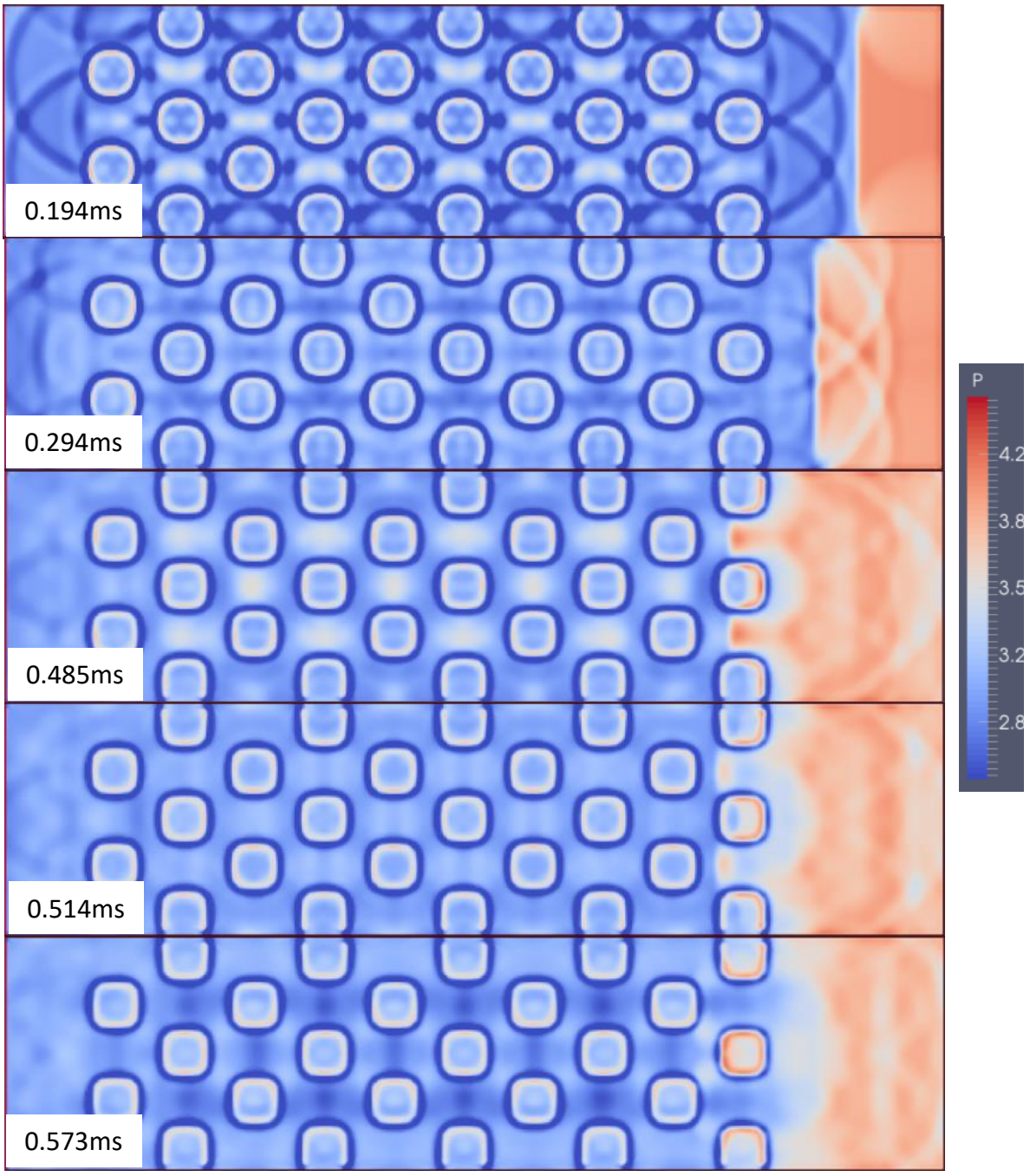

Figure 14: 25 bubble pressure surge simulation, 0.194 ms to 0.573 ms

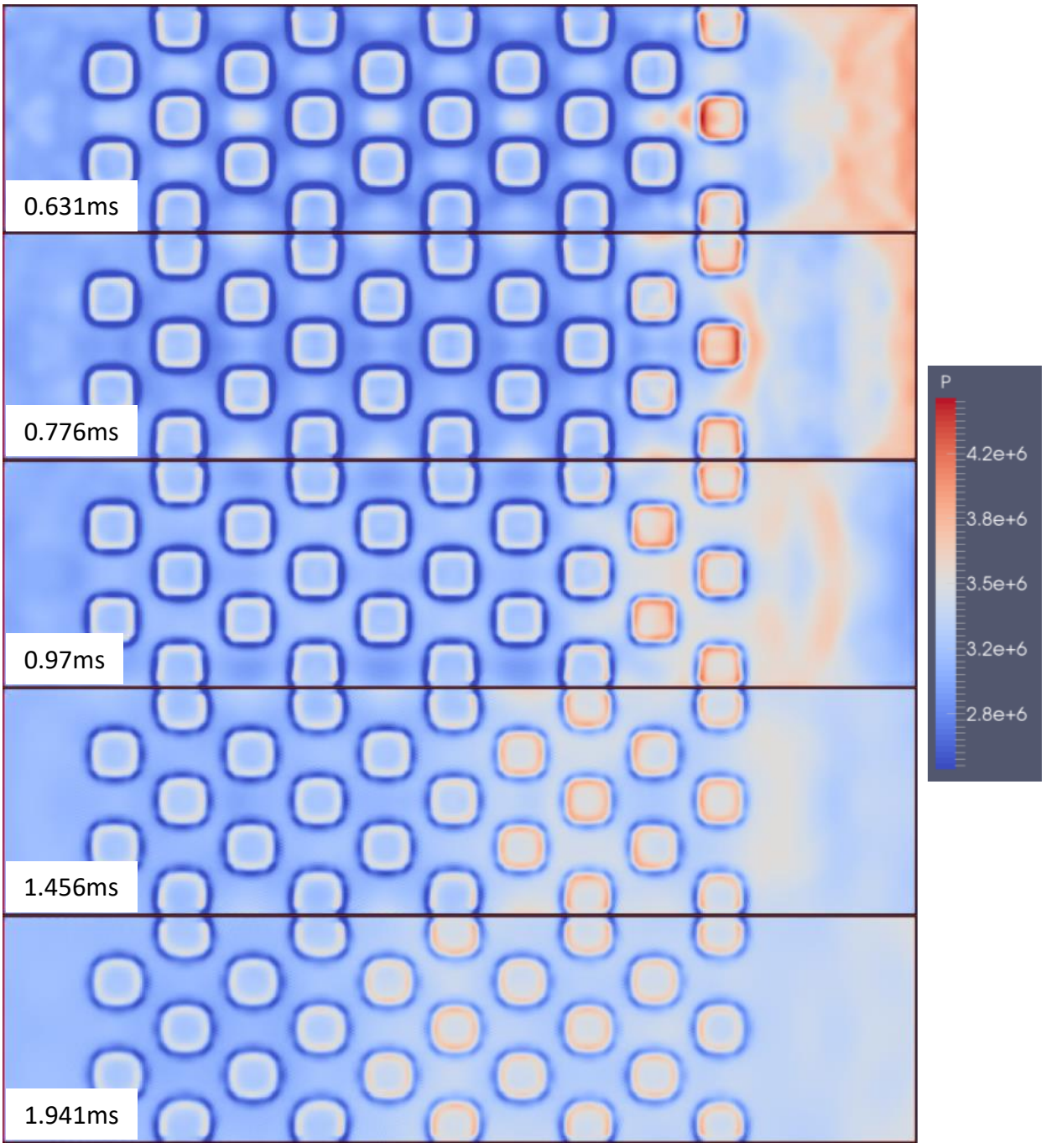

Figure 15: 25 bubble pressure surge simulation, 0.631 ms to 1.941 ms

4 Conclusion and Outlook

This work investigated the suitability of the Lattice Boltzmann Method (LBM) for applications in rocket engines. Rocket engines have a unique set of challenges which need to be mastered by a numerical method in order to supply useful results. The main focus was on the fluid supply system guiding cryogenic propellants like liquid oxygen and liquid methane to the combustion chamber. Here evaporation takes place in the chilldown phase, which is prior to the start of the engine. Fast valve movements might lead to pressure surges in the system. For this reason, a thermal two-phase model of the LBM was chosen from literature which uses a multi-speed finite difference approach and an additional force term. Its applicability to the aforementioned phenomena was investigated by a set of validation cases.

It was shown that the model reproduces the flow in a driven cavity very well, it is well suited to numerically simulate evaporation on heated surfaces and it reproduces the main flow features of a Riemann shock tube with low errors.

Three pressure surge simulations with liquid nitrogen have been performed. In the simulation of a single-phase liquid, the LBM performs well in predicting the speed of sound and it has overall stability, while showing minor shortcomings in the pressure attenuation and the maximum pressure peak of the pressure surge.

Finally, a duct filled with bubbles was simulated. Strong pressure wave attenuation is observed due to multiple wave scattering in the bubble cloud.

For future works it is suggested to look into another real gas model, since the model used only obeys the equation of state of a van-der-Waals gas. Moreover, the stability of this model is limited and the wave attenuation in pressure surge simulation was found to be too high.

For evaporation of LOX at a wall the contact angle needs to be measured by experiments and adjusted in the model to the specific problem under investigation.

All in all, the LBM simulations of the validation cases showed, that LBM is applicable to the physical challenges associated with fluid flows in rocket engines. Great care needs to be taken to set up the simulation since the LBM equations describe their very own fluid and the physical fluid properties need to be mapped via similarity laws to the LBM properties. This is done via non-dimensional numbers like the well-known Reynolds-number, for example and by the so-called corresponding states principle. The latter is only accurate for single atomic gases (only noble gases basically) and deviates more and more the more asymmetrical the fluid molecules become.

5 References

Alexander, F. J., Chen, S. & Sterling, J. D., 1993. Lattice Boltzmann thermohydrodynamics. *Phys. Rev. E,* Apr, Volume 47, pp. R2249--R2252.

Begun, R. & Basit, M. A., 2008. Lattice Boltzmann Method and its Applications to Fluid Flow Problems. *European Journal of Scientific Research,* Volume 22, pp. 216-231.

Biferale, L. et al., 2012. An optimized D2Q37 Lattice Boltzmann code on GP-GPUs. *Computers \& Fluids,* Issue 0.

Biggs, R. E., 1989. *Space Shuttle Main Engine, The First Ten Years.* s.l., s.n.

Brennen, C. E., 2005. *Fundamentals of Multiphase Flows.* s.l.:Cambridge University Press.

Buwa, V., Donath, S., Swapna, R. & Rüde, U., 2010. *Lattice Boltzmann simulation of bubbly flows: First results of experimental verification and comparison with Volume of Fluid model,* s.l.: s.n.

Chen, S. & Doolen, G. D., 1998. Lattice Boltzmann Method for Fluid Flows. *Ann. Rev. Fluid Mech.,* Volume 30, pp. 329-364.

Chung, T., 2002. *Computational Fluid Dynamics.* s.l.:Cambridge University Press.

Cristea, A., Gonnella, G., Lamura, A. & Sofonea, V., 2006. Finite-difference lattice Boltzmann model for liquid–vapor systems.

Mathematics and Computers in Simulation, Volume 72, pp. 113-116.

Cristea, A. & Sofonea, V., 2004. Two component lattice Boltzmann model with flux limiters. *Central European Journal of Physics,* Volume 2, pp. 382-396.

Frisch, U., Hasslacher, B. & Pomeau, Y., 1986. Lattice-Gas Automata for the Navier-Stokes Equation. *Phys. Rev. Lett.,* Apr, Volume 56, pp. 1505-1508.

Gan, Y. et al., 2012. Lattice Boltzmann study of thermal phase separation: Effects of heat conduction, viscosity and Prandtl number. *EPL (Europhysics Letters),* 97(4), p. 44002.

Ghia, U., Ghia, K. N. & Shin, C. T., 1982. High-Re solutions for incompressible flow using the Navier-Stokes equations and a multigrid method. *Journal of Computational Physics,* Volume 48, pp. 387-411.

Giordano, J. & Burtschell, Y., 2006. Richtmyer-Meshkov instability induced by shock-bubble interaction: Numerical and analytical studies with experimental validation. *Physics of Fluids,* Volume 18, p. 036102.

Gonnella, G., Lamura, A., Piscitelli, A. & Tiribocchi, A., 2010. Phase separation of binary fluids with dynamic temperature. *Phys. Rev. E,* Oct, Volume 82, p. 046302.

Gonnella, G., Lamura, A. & Sofonea, V., 2007. Lattice Boltzmann simulation of thermal nonideal fluids. *Phys. Rev. E,* Sep, Volume 76, p. 036703.

He, X. & Doolen, G. D., 2002. Thermodynamic Foundations of Kinetic Theory and Lattice Boltzmann Models for Multiphase Flows. *Journal of Statistical Physics,* Volume 107, pp. 309-328.

Huang, H., Sukop, M. C. & Lu, X.-Y., 2015. Multiphase Lattice Boltzmann Methods: Theory and Application. June.

Junk, M., Klar, A. & Luo, L.-S., 2005. Asymptotic analysis of the lattice Boltzmann equation. *Journal of Computational Physics,* 210(2), pp. 676-704.

Kalarakis, A. N., Burganos, V. N. & Payatakes, A. C., 2002. Galilean-invariant lattice-Boltzmann simulation of liquid-vapor interface dynamics. *Phys. Rev. E,* Apr, Volume 65, p. 056702.

Kupershtokh, A., Medvedev, D. & Karpov, D., 2009. On equations of state in a lattice Boltzmann method. *Computers \& Mathematics with Applications,* 58(5), pp. 965-974.

Leighton, T. G., 1994. In: *The Acoustic Bubble.* s.l.:Academic Press.

Lou, Q., Guo, Z. & Shi, B., 2013. Evaluation of outflow boundary conditions for two-phase lattice Boltzmann equation. *Phys. Rev. E,* Jun, 87(6), p. 063301.

Mukherjee, A. & Dhir, V. K., 2004. Study of Lateral Merger of Vapor Bubbles During Nucleate Pool Boiling. *Journal of Heat Transfer,* January, Volume 126, p. 1023–1039.

National Institute of Standards and Technology, 2018. *Thermophysical Properties of Fluid Systems.* https://webbook.nist.gov/chemistry/fluid/, s.n.

Pfister, M. & Hager, W. H., 2014. History and Significance of the Morton Number in Hydraulic Engineering. *Journal of Hydraulic Engineering,* May.Volume 140.

Philippi, P. C., Hegele, L. A., E., L. O. & Surmas, R., 2006. From the continuous to the lattice Boltzmann equation: The discretization problem and thermal models. *Phys. Rev. E,* May, Volume 73, p. 056702.

Sbragaglia, M. et al., 2009. Lattice Boltzmann method with self-consistent thermo-hydrodynamic equilibria. *Journal of Fluid Mechanics,* #jun#, Volume 628, p. 299.

Scagliarini, A. et al., 2010. Lattice Boltzmann methods for thermal flows: Continuum limit and applications to compressible Rayleigh-Taylor systems. *Physics of Fluids,* #may#, 22(5), p. 055101.

Shan, X. & Chen, H., 1993. Lattice Boltzmann model for simulating flows with multiple phases and components. *Physical Review,* Volume 47, pp. 1815-1820.

Shan, X. & Chen, H., 1994. Simulation of nonideal gases and liquid-gas phase transitions by the lattice Boltzmann equation. *Phys. Rev. E,* Apr, Volume 49, pp. 2941-2948.

Slater, J. W., 2015. *NASA NPARC Alliance Verification and Validation Archive.* s.l.:s.n.

Sofonea, V., 2009. Implementation of diffuse reflection boundary conditions in a thermal lattice Boltzmann model with flux limiters. *Journal of Computational Physics,* 228(17), pp. 6107-6118.

Sofonea, V. & Sekerka, R. F., 2003. Viscosity of finite difference lattice Boltzmann models. *Journal of Computational Physics,* 184(2), pp. 422-434.

Sukop, D. T., 2006. *Lattice Boltzmann Modelling.* s.l.:Springer Verlag.

Surmas, R., Pico, C. E. & Philippi, P. C., 2009. Simulating thermohydrodynamics by finite difference solutions of the Boltzmann equation. *The European Physical Journal Special Topics,* Volume 171, pp. 81-90.

Swift, M. R., Orlandini, E., Osborn, W. R. & Yeomans, J. M., 1996. Lattice Boltzmann simulations of liquid-gas and binary fluid systems. *Phys. Rev. E,* Nov, Volume 54, pp. 5041-5052.

Tölke, J., 2001. *Gitter-Boltzmann-Verfahren zur Simulation von Zweiphasenströmung,* s.l.: s.n.

Traudt, T., Bombardieri, C. & Manfletti, C., 2015. *High Speed Imaging of Water Hammer with Column Separation.* s.l., s.n.

Vincenti, W. & Kruger, C., 1975. *Realgasdynamik.* s.l.:Krieger Publishing Company.

Wagner, J., 2005. *Dynamik I.* s.l.:ISD, Universität Stuttgart.

Watari, M., 2007. Finite difference lattice Boltzmann method with arbitrary specific heat ratio applicable to supersonic flow simulations. *Physica A: Statistical Mechanics and its Applications,* Volume 382, pp. 502-522.

Watari, M., 2009. Velocity slip and temperature jump simulations by the three-dimensional thermal finite-difference lattice Boltzmann method. *Phys. Rev. E,* Jun, Volume 79, p. 066706.

Watari, M. & Tsutahara, M., 2003. Two-dimensional thermal model of the finite-difference lattice Boltzmann method with high spatial isotropy. *Phys. Rev. E,* Mar, Volume 67, p. 036306.

Watari, M. & Tsutahara, M., 2006. Supersonic flow simulations by a three-dimensional multispeed thermal model of the finite difference lattice Boltzmann method. *Physica A: Statistical Mechanics and its Applications,* 364(0), pp. 129-144.

Xiang, H. W., 2005. *The Corresponding-States Principle and its Practice.* s.l.:Elsevier B.V..

Yuan, P. & Schäfer, L., 2006. A Thermal Lattice Boltzmann Two-Phase Flow Model and Its Application to Heat Transfer Problems—Part 2. Integration and Validation. *Journal of Fluids Engineering,* Volume 128, pp. 151-156.

Yuan, P. & Schäfer, L., 2006. Equations of state in a lattice Boltzmann model. *Physics of Fluids,* Volume 18, pp. 1-11.

Zhang, J., Li, B. & Kwok, D. Y., 2004. Mean-field free-energy approach to the lattice Boltzmann method for liquid-vapor and solid-fluid interfaces. *Phys. Rev. E,* Mar, Volume 69, p. 032602.

Zhang, R. & Chen, H., 2003. Lattice Boltzmann method for simulations of liquid-vapor thermal flows. *Phys. Rev. E,* Jun, Volume 67, p. 066711.